

# Chapter 2

## Study of Systematic Contributions via Numerical Simulations

It has been observed that a unipolar non-reversing electric fields ( $\mathcal{E}_{\text{nr}}$ ) centered at Gap 22, coupled with the 2nd depletion laser detuning offset ( $\delta_{L2}$ ), can imitate a NSD-PV signal. The unipolar  $\mathcal{E}_{\text{nr}}$  pulse centered around other gaps exhibit no similar systematic offset. To be specific, linear relationships

$$W = C_W \times (\mathcal{E}_{\text{nr},0} \cdot \delta_{L2}) \quad (2.1)$$

$$a_0 = C_{a_0} \times \mathcal{E}_{\text{nr},0} \quad (2.2)$$

$$a_1 = C_{a_1} \times (\mathcal{E}_{\text{nr},0} \cdot \delta_{L2}) \quad (2.3)$$

were observed from the experiment only when  $\mathcal{E}_{\text{nr}}$  is at Gap 22, and there wasn't any satisfactory model for an underlying physical mechanism that captures all observed features of this effect. In the equation,  $\mathcal{E}_{\text{nr},0}$  is the non-reversing field strength.

To understand this systematic errors and thus reduce them, we conducted numerical simulations of our system.

(Backgrounds, importance, previous results, methods, chapter layout.)

## 2.1 Numerical Simulation

The simulation algorithm presented here is developed through numerical integration of the optical Bloch equations (OBE) for an equivalent three-level molecular system. This system models the interaction dynamics among the even-parity ground state  $X^2\Sigma(v = 0, N^P = 0^+, J = 1/2)$ , the odd-parity ground state  $X^2\Sigma(v = 0, N^P = 1^-, J = 3/2)$ , and a short-lived electronic state of even-parity excited state  $A^2\Pi_{1/2}(J^P = 5/2^+)$  with a decay rate  $\Gamma = 2.7 \times 2\pi$  MHz.

Since systematic effects due to magnetic field ( $\mathcal{B}$ -field) inhomogeneities are well characterized, we neglect any spatial variation of the  $\mathcal{B}$ -field within the interaction region in this chapter by assuming the magnetic field is constant throughout this region. Then, the effect of a constant  $\mathcal{B}$ -field manifests simply as energy shifts of the molecular states due to the Zeeman effect. In our simulation, the constant  $\mathcal{B}$ -field can be effectively incorporated into the model by adjusting the energy detuning between the two ground states, allowing us to explicitly set  $\mathcal{B} = 0$  and control the energy detuning between the two opposite parity ground states  $\Delta$  instead.

### 2.1.1 Electric Fields

In an ideal world, as the molecular beam traverses the interaction region, it encounters three distinct electric fields:

1. The first depletion laser L1 field ( $\mathcal{E}_{L1}$ ), which depletes the detection state (even-parity ground state) via optical pumping while leaving the non-detection state (odd-parity ground state) populated.
2. The Stark interference field ( $\mathcal{E}_{\text{stark}}$ ), a single cycle sine wave that induces a small population transfer from the non-detection state back into the detection state.
3. The second depletion laser L2 field ( $\mathcal{E}_{L2}$ ), which optically pumps any remaining population out of the non-detection state.

However, due to the imperfections of the apparatus, small stray electric field is unavoidable. In this chapter, we will specifically consider a stray field in a form of an unipolar non-reversing field  $\mathcal{E}_{\text{nr}}$ . We include an intentionally amplified  $\mathcal{E}_{\text{nr}}$  in the model to simulate the effect of it to the system. Given the assumption of perfect optical pumping efficiency by the L1 laser, L1 laser can be effectively omitted from simulation by setting the initial conditions to be a fully populated even-parity ground state.

Note that both  $\mathcal{E}_{\text{nr}}$  and  $\mathcal{E}_{\text{stark}}$  are spatially varying but time-independent fields in the lab frame. However, in the molecule's moving frame, the spatial variation translates into a time-dependent field through the simple conversion  $t = x/v$ , where  $v = 616 \text{ m/s}$  is the molecular beam velocity. In contrast,  $\mathcal{E}_{\text{L2}}$  is inherently time-dependent field because it is a high-frequency excitation (2nd depletion laser frequency  $\omega_{\text{L2}} \approx 348.69 \text{ THz}$ ), and the linear motion of the molecule induced Doppler shift is negligible in this treatment. Throughout this chapter, all electric fields will be presented explicitly as functions of time in the molecular beam frame.

In summary, our model treats the molecular system as a three-level quantum system, two stable ground states with opposite parity with a short-lived even parity excited state with a decay rate  $\Gamma/2\pi = 2.7 \text{ MHz}$ , interacting with three time-dependent electric fields:  $\mathcal{E}_{\text{stark}}(t)$ ,  $\mathcal{E}_{\text{L2}}(t)$ , and  $\mathcal{E}_{\text{nr}}(t)$ , whose time-dependent functional forms are defined as follows:

$$\mathcal{E}_{\text{stark}}(t) = \mathcal{E}_0 \sin(\omega t), \quad -43.7 \mu\text{s} < t < 43.7 \mu\text{s} \quad (2.4)$$

$$\mathcal{E}_{\text{nr}}(t) = \mathcal{E}_{\text{nr},0} \operatorname{sech}\left(\frac{v(t - t_{\text{nr}})}{\sigma_u}\right) \quad (2.5)$$

$$\mathcal{E}_{\text{L2}}(t) = \mathcal{E}_{\text{L2},0}(t) \cos(\omega_{\text{L2}} t), \quad 51.85 \mu\text{s} < t < 53.35 \mu\text{s} \quad (2.6)$$

where  $\mathcal{E}_{\text{L2},0}(t)$  is the time dependent 2nd depletion laser amplitude which we modeled as a Gaussian function in time domain. Test simulations show that approximating the laser intensity as a flat-top profile introduces a significant change in the simulation result, likely due to the higher frequency excitations generated by the artificial sharp edges that couples

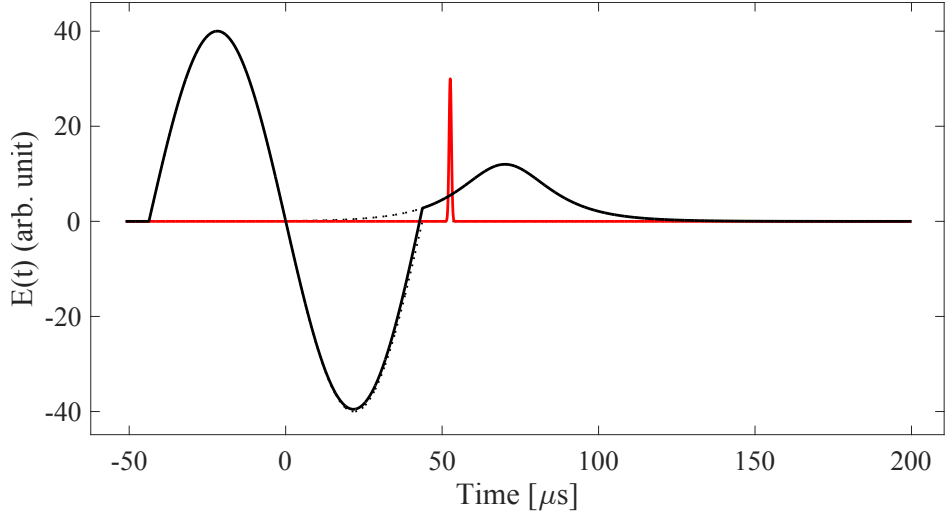


Figure 2.1: Electric field profiles illustration in the molecular-beam frame. The solid black trace shows the combined static fields (Stark field  $\mathcal{E}_{\text{stark}}$  plus stray non-reversing field  $\mathcal{E}_{\text{nr}}$ ) which, although time-independent in the laboratory, appear here as a function of time via the conversion  $t = x/v$  ( $v = 616$  m/s). The red curve is the Gaussian-shaped amplitude envelope of the 2nd depletion laser pulse (oscillations omitted), as defined in Eqn. (2.6). The dotted black lines indicate what the  $\mathcal{E}_{\text{nr}}$  and  $\mathcal{E}_{\text{stark}}$  would have looked like independently, as defined in Eqn. (2.5) and Eqn. (2.4). Both traces are plotted in arbitrary units and are not to scale.

the levels.  $\sigma_u$  is the width constant of the non-reversing field. Coming out of the polarization maintaining fiber, the 2nd depletion laser beam is first collimated by an aspherical lens to a  $1/e^2$  diameter of 0.92 mm. A cylindrical lens subsequently expands the beam in the vertical direction, resulting in a vertical  $1/e^2$  diameter of 11.5 mm. This choice was made so that the half maximum power width of the laser beam is equal to the molecular beam size at center of the IR, which diminish differences between the laser intensity seen by the molecules on the edges of the beam and the ones at the center area, while not sacrificing too much laser power. Since the molecular beam propagates horizontally, the laser intensity encountered by a molecule varies in time as a Gaussian profile in the molecule's frame. The temporal width (standard deviation) of this Gaussian is given by  $\sigma_{L2} = d/(4v) = 0.373\mu\text{s}$ , where  $d$  is the horizontal beam diameter and  $v$  is the molecular beam velocity. Therefore, the time-dependent 2nd depletion laser strength envelope is expressed as:

$$\mathcal{E}_{L2,0}(t) = \mathcal{E}_{L2,\max} e^{-(t-t_{L2,0})^2/\sigma_{L2}^2} \quad (2.7)$$

where  $t_{L2,0}$  is the center arrival time of the L2 pulse, and  $\mathcal{E}_{L2,\max}$  is its peak amplitude. In the experiment, we use a depletion laser with 8mW of power, let  $I_{\max}$  be the peak power of the laser,

$$P = I_{\max} \int_{-\infty}^{\infty} \int_{-\infty}^{\infty} e^{-x^2/2\sigma_x^2} e^{-y^2/2\sigma_y^2} dx dy = 2\pi I_{\max} \sigma_x \sigma_y = 8 \text{ mW} \quad (2.8)$$

where  $\sigma_x, \sigma_y$  are spacial variance of the laser along horizontal and vertical direction. Plug into the numbers, and use classic electrodynamics, we obtain

$$\mathcal{E}_{L2,\max} = \sqrt{\frac{2I_{\max}}{\epsilon_0 c}} = 1204.1 \text{ V/m}, \quad (I_{\max} = 1925.5 \text{ W/m}^2) \quad (2.9)$$

### 2.1.2 Optical Bloch Equations and An Equivalent Schrödinger equation with a Non-Hermitian Hamiltonian

It is convenient to define the total field as the sum of these individual fields:

$$\mathcal{E}(t) = \mathcal{E}_{\text{stark}}(t) + \mathcal{E}_{\text{nr}}(t) + \mathcal{E}_{L2}(t). \quad (2.10)$$

Define the state vector that describes the three level system,

$$|\Psi(t)\rangle = \begin{pmatrix} \text{even parity ground state} \\ \text{odd parity ground state} \\ \text{excited state} \end{pmatrix} = \begin{pmatrix} c_+(t) \\ c_-(t) \\ c_e(t) \end{pmatrix} \quad (2.11)$$

The Hamiltonian governing this three-level system can then be expressed as:

$$\mathcal{H}(t) = \begin{pmatrix} 0 & iW + d_{12} \cdot \mathcal{E}(t) & d_{23} \cdot \mathcal{E}(t) \\ -iW + d_{12} \cdot \mathcal{E}(t) & \Delta & d_{13} \cdot \mathcal{E}(t) \\ d_{23} \cdot \mathcal{E}(t) & d_{13} \cdot \mathcal{E}(t) & \Delta_{13} \end{pmatrix} \quad (2.12)$$

where  $d_{12}$ ,  $d_{13}$ , and  $d_{23}$  are dipole matrix elements connecting the odd-parity ground state with the even-parity ground state, the odd-parity ground state with the excited state, and the even-parity ground state with the excited state, respectively. The selection rule dictates that  $d_{23} = 0$ . Additionally,  $\Delta$  represents the energy detuning between the two ground states of opposite parity, while  $\Delta_{13}$  is the energy difference between the odd-parity ground state and the excited state.

In the density matrix formalism, the optical Bloch equations (OBEs) describe the time evolution of the density matrix  $\rho(t) = |\Psi(t)\rangle\langle\Psi(t)|$  for a three-level system under laser drive and spontaneous emission

$$\frac{d\rho(t)}{dt} = -i[\mathcal{H}'(t), \rho(t)] + \mathcal{L}(\rho(t)) \quad (2.13)$$

describes the dissipative (non-unitary) dynamics, specifically the population decay from the short-lived excited state to states outside the system:

$$\mathcal{L}(\rho) = \begin{pmatrix} 0 & 0 & -\frac{\Gamma}{2}\rho_{13} \\ 0 & 0 & -\frac{\Gamma}{2}\rho_{23} \\ -\frac{\Gamma}{2}\rho_{31} & -\frac{\Gamma}{2}\rho_{32} & -\Gamma\rho_{33} \end{pmatrix}. \quad (2.14)$$

Direct numerical integration of these OBE can be computationally challenging due to rapidly oscillating terms, particularly from  $\mathcal{E}_{L2}(t)$ , and most ODE solver just can't handle this kind of difference in magnitude of the frequencies between three fields. Therefore, moving into a rotating frame is necessary. Transforming Hamiltonian into a rotating frame can be

done by an unitary transformation,

$$\mathcal{H}'(t) = U^\dagger(t) H(t) U(t) - i U^\dagger(t) \frac{dU(t)}{dt} \quad (2.15)$$

with  $U(t) = \text{diag}(1, 1, e^{-i\omega_{L2}t})$ . The transformed  $\mathcal{H}'(t)$ . The resulting Hamiltonian  $H'(t)$  becomes:

$$\mathcal{H}'(t) = \begin{pmatrix} 0 & iW + d_{12} \cdot \mathcal{E}(t) & 0 \\ -iW + d_{12} \cdot \mathcal{E}(t) & \Delta & d_{13} \cdot \mathcal{E}(t) e^{-i\omega_{L2}t} \\ 0 & d_{13} \cdot \mathcal{E}(t) e^{i\omega_{L2}t} & \delta_{L2} \end{pmatrix} \quad (2.16)$$

where  $\delta_{L2} \equiv \Delta_{13} - \omega_{L2}$  is the 2nd depletion laser detuning. Recall  $\cos(\omega_{L2}t) = (e^{i\omega_{L2}t} + e^{-i\omega_{L2}t})/2$ , apply rotating wave approximation gives,

$$\begin{aligned} \mathcal{E}(t) \cdot e^{-i\omega_{L2}t} &= \left( \mathcal{E}_{\text{stark}}(t) + \mathcal{E}_{\text{nr}}(t) + \mathcal{E}_{L2,0}(t) \cdot \left( \frac{e^{i\omega_{L2}t} + e^{-i\omega_{L2}t}}{2} \right) \right) \cdot e^{-i\omega_{L2}t} \\ &\approx (\mathcal{E}_{\text{stark}}(t) + \mathcal{E}_{\text{nr}}(t)) \cdot e^{-i\omega_{L2}t} + \frac{\mathcal{E}_{L2,0}(t)}{2} \\ &\approx \frac{\mathcal{E}_{L2,0}(t)}{2} \end{aligned}$$

and

$$d_{12} \cdot \mathcal{E}(t) \approx d_{12} \cdot \left( \mathcal{E}_{\text{stark}}(t) + \mathcal{E}_{\text{nr}}(t) \right) \equiv d_{12} \cdot \mathcal{E}_{nL2}(t)$$

Hence, the simplified rotating frame Hamiltonian reads

$$\mathcal{H}'(t) \approx \begin{pmatrix} 0 & \Omega_{12}(t) & 0 \\ \Omega_{12}(t)(t) & \Delta & \frac{1}{2}\Omega_{13}(t) \\ 0 & \frac{1}{2}\Omega_{13}(t) & \delta_{L2} \end{pmatrix} \quad (2.17)$$

where  $\Omega_{12}(t) \equiv d_{12} \cdot \mathcal{E}_{nL2}(t)$  and  $\Omega_{13}(t) \equiv d_{13} \cdot \mathcal{E}_{L2,0}(t)$ .

To further simplify the OBE, we introduce an equivalent non-Hermitian Hamiltonian

(NHH)  $\mathcal{H}_N(t)$ , absorbing dissipation directly into the Hamiltonian

$$\frac{d\rho}{dt} = -i[\mathcal{H}_N, \rho] = -i(\mathcal{H}_N\rho - \rho\mathcal{H}_N^\dagger) \quad (2.18)$$

Where the commutation relation has been modified for a NHH in order to make sure that the density matrix remains Hermitian  $\rho = \rho^\dagger$ . I've set  $\mathcal{H}_N = \mathcal{H}_N(t)$  etc. until the end of this section to make equations looks cleaner. This  $\mathcal{H}_N(t)$  can found by observing that

$$\mathcal{L}(\rho) = \begin{pmatrix} 0 & 0 & -\frac{\Gamma}{2}\rho_{13} \\ 0 & 0 & -\frac{\Gamma}{2}\rho_{23} \\ -\frac{\Gamma}{2}\rho_{31} & -\frac{\Gamma}{2}\rho_{32} & -\Gamma\rho_{33} \end{pmatrix} \quad (2.19)$$

$$= -\frac{\Gamma}{2}[|3\rangle\langle 3| \cdot \rho + \rho \cdot |3\rangle\langle 3|] \quad (2.20)$$

$$= -\frac{\Gamma}{2}\{|3\rangle\langle 3|, \rho\} \quad (2.21)$$

let's write  $\mathcal{H}_N = \mathcal{H}_{N,r} + i\mathcal{H}_{N,i}$ , then

$$[\mathcal{H}_N, \rho] = [\mathcal{H}_{N,r}, \rho] + [i\mathcal{H}_{N,i}, \rho] \quad (2.22)$$

$$= [\mathcal{H}_{N,r}, \rho] + i(\mathcal{H}_{N,i}\rho + \rho\mathcal{H}_{N,i}) \quad (2.23)$$

$$= [\mathcal{H}_{N,r}, \rho] + i\{\mathcal{H}_{N,i}, \rho\} \quad (2.24)$$

where in second line I have used the modified commutation relation. Thus, we have

$$\frac{d\rho}{dt} = -i[\mathcal{H}', \rho] - \frac{\Gamma}{2}\{|3\rangle\langle 3|, \rho\} = -i[\mathcal{H}_{H,r}, \rho] + \{\mathcal{H}_{N,i}, \rho\} \quad (2.25)$$

Comparing Eqn. (2.13) and Eqn. (2.25) gives  $\mathcal{H}_{N,r} = \mathcal{H}'$ ,  $\mathcal{H}_{N,i} = -\frac{\Gamma}{2}|3\rangle\langle 3|$ , or

$$\mathcal{H}_N = \mathcal{H}' - i\frac{\Gamma}{2}|3\rangle\langle 3| = \begin{pmatrix} 0 & \Omega_{12}(t) & 0 \\ \Omega_{12}(t) & \Delta & \frac{1}{2}\Omega_{13}(t) \\ 0 & \frac{1}{2}\Omega_{13}(t) & \delta_{L2} - i\frac{\Gamma}{2} \end{pmatrix} \quad (2.26)$$

Now, solving the OBEs becomes equivalent to solving the Schrödinger equation with a non-Hermitian Hamiltonian,

$$\frac{\partial\Psi(t)}{\partial t} = -i\mathcal{H}_N(t)\Psi(t) \quad (2.27)$$

with initial condition

$$|\Psi(t=0)\rangle = \begin{pmatrix} 0 \\ 1 \\ 0 \end{pmatrix} \quad (2.28)$$

where  $t = 0$  is defined to be the time when the first depletion laser L1 applied. In our simulation, both the OBE approach and the Schrödinger equation with a non-Hermitian Hamiltonian method have been implemented and yield identical results. However, due to computational efficiency, the Schrödinger equation method is predominantly employed.

## 2.2 Systematic Error Due to the Combination of 2nd Depletion Laser Detuning Offset $\delta_{L2}$ and Unipolar Non-Reversing Electric Field $\mathcal{E}_{nr}$ at Gap 22

Previous experiments have revealed a systematic shift in the induced matrix element  $W$ , attributed to the combined presence of the non-resonant field  $\mathcal{E}_{nr}$  near the second depletion laser beam (i.e., at Gap 22) and a non-zero detuning offset of the second depletion laser,  $\delta_{L2}$ . However, a comprehensive theoretical model that fully accounts for all observed features of this effect remains elusive. In this section, we first use numerical simulations based on the

optical Bloch equations developed earlier Eqn. (2.27) to attempt to reproduce the observed systematic shift in section (2.2.1). We then seek to derive an analytical expression for the systematic shift in  $W$  as a function of relevant experimental parameters in section (2.2.2).

To maintain consistency in notation, we define the origin  $t = 0$  to be the center of the interaction region (IR). The initial time in the simulation is  $t_{L1} = -51.1, \mu\text{s}$ , which corresponds to the moment when the first depletion laser projects the population into parity eigenstates. The initial condition is then given by  $c_+(t) = 0$ ,  $c_-(t) = 1$ , and  $c_e(t) = 0$ , meaning the system starts in a pure odd-parity ground state at start.

Experimental geometry defines the electric field boundaries: the Stark field  $\mathcal{E}_0$  is non-zero only in the spatial region  $-2.69, \text{cm} \leq z \leq 2.96, \text{cm}$ . With molecular beam velocity  $v = 616, \text{m/s}$ , this translates into the temporal interval  $-43.7, \mu\text{s} \leq t \leq 43.7, \mu\text{s}$ . The second depletion laser (L2) is located at  $t_{L2} = +52.6, \mu\text{s}$ . The non-reversing field  $\mathcal{E}_{\text{nr}}$  is centered at Gap 22, which corresponds to  $z_{22} = +4.32, \text{cm}$  or  $t_{\text{nr}} = +70.1, \mu\text{s}$ , and has a spatial width of  $\sigma_u = 7.6, \text{mm}$ . The full simulation window spans from  $t_{L1} = -51.1 \mu\text{s}$  to  $T_{\text{final}} = 200 \mu\text{s}$ , ensuring complete coverage of  $\mathcal{E}_{\text{nr}}$ . Some preliminarily numerical tests confirm that extending the  $T_{\text{final}}$  further has negligible impact on results. We define the free evolution times as  $T_{f1} = 7.4, \mu\text{s}$  and  $T_{f2} = 8.9, \mu\text{s}$ , representing the intervals between L1 and the Stark field, and between the Stark field and L2, respectively. While these parameters reflect the actual experimental setup, some of them are treated as tunable variables in the second part of the simulation to explore possible mechanisms for the observed systematic shifts. The simulation results with those experimentally realistic values as inputs are used to compare with the experimental data.

Schrödinger equation with non-Hermitian Hamiltonian is then solved to extract the amplitude  $c_+(t)$  of the even-parity ground state as a function of the detuning  $\Delta$  between the parity eigenstates. This provides the detection signal  $S(\pm\mathcal{E}_0)$ , from which the simulated asymmetry is calculated

$$\mathcal{A}(\Delta) = \frac{S(+\mathcal{E}_0) - S(-\mathcal{E}_0)}{S(+\mathcal{E}_0) + S(-\mathcal{E}_0)} \quad (2.29)$$

The simulated asymmetry data is then fitted using

$$\mathcal{A}_{\text{fit}}(\Delta) = 2 \frac{W}{\Delta} \frac{\omega^2 - \Delta^2 \sin\left[\frac{\Delta}{2}(T_e + T_{f_1} + T_{f_2})\right]}{d_{12} \cdot \mathcal{E}_0 \omega \sin(\Delta T_e / 2)} \cos\left[\frac{\Delta}{2}(T_{f_1} - T_{f_2})\right] + a_0 + a_1 \cdot \Delta \quad (2.30)$$

with  $W$ ,  $a_0$ , and  $a_1$  as free parameters in the fits. In the fitting function,  $T_e = 87.4 \mu\text{s}$  is the duration of the Stark interaction, and  $\omega/(2\pi) = 1/T_e = 11.4 \text{ kHz}$ . Since  $W$  is set to zero in the Hamiltonian, any non-zero  $W$  extracted from the fit is interpreted as arising from systematic effects.  $a_0, a_1$  are constants that accounts for the observation of a vertical offset in asymmetry and an offset that goes linearly with the energy detuning between two opposite parity ground states  $\Delta$ , respectively, from both previous experiment and simulation results. Fitting is restricted to the detuning range  $1 \text{ kHz} \leq |\Delta/(2\pi)| \leq 4 \text{ kHz}$  to avoid regions with high statistical noise due to low transition probability. The fitting uses a nonlinear least-squares method, minimizing the sum of squared residuals between the simulated asymmetry and the theoretical model using Matlab's `fminsearch` routine. Understanding the role of those fitting parameters plays in the experiment and the physics mechanisms that give rise to their relationships is the goal of this chapter.

Table (2.1) summarizes all relevant parameters used in the simulation and experiment. Values in parentheses indicate the maximum range explored in the simulations.

### 2.2.1 Simulation Result

#### Reproducing The Error Signal with a Reduced Laser Intensity

This part of the numerical simulation tries to reproduce the systematic error showed up in the experiment presented in Emine's thesis Figure (7.9) - (7.11). The electric field excitation is defined in Eqn. (2.4)-(2.6). In this part, all the simulations will start at  $t_{L1} = -51.1 \mu\text{s}$  and ends at  $t = 200 \mu\text{s}$ , given the usual definition for free evolution durations  $T_{f1} = 7.4 \mu\text{s}$ ,  $T_{f2} = 8.9 \mu\text{s}$ . As mentioned before, this end time is chosen so that the molecule run through all the non-trivial parts of  $\mathcal{E}_{\text{nr}}$  while maintain a reasonable computation time.

Description	Symbol	Value	Unit
Weak Matrix Element	$W$	0	Hz
Stark Field Strength	$\mathcal{E}_0$	40	V/m
NR Field Strength	$\mathcal{E}_{\text{nr},0}$	(12)	V/m
2nd depletion laser Field Strength	$\mathcal{E}_{L2,0}$	1204.1	V/m
Dipole Matrix Element ( $1 \leftrightarrow 2$ )	$d_{12}$	$-33.6 \times 2\pi$	rad/(s·V/m)
Dipole Matrix Element ( $1 \leftrightarrow 3$ )	$d_{13}$	$-2.15 \times 10^4 \times 2\pi$	rad/(s·V/m)
Interaction Time	$T_e$	$87.4 \times 10^{-6}$	s
Free Evolution Time After L1	$T_{f1}$	$7.4 \times 10^{-6}$	s
Free Evolution Time Before L2	$T_{f2}$	$8.9 \times 10^{-6}$	s
L1 Laser Center Location	$t_{L1}$	$-51.1 \times 10^{-6}$	s
2nd depletion laser Center Location	$t_{L2}$	$+52.6 \times 10^{-6}$	s
NR Field Center Location	$t_{\text{nr}}$	$+70.1 \times 10^{-6}$	s
Excited State Decay Rate	$\Gamma$	$2.7 \times 10^6 \times 2\pi$	rad/s
Stark Field Angular Frequency	$\omega$	$11.44 \times 10^3 \times 2\pi$	rad/s
Molecular Beam Velocity	$v$	616	m/s
NR Field Width Constant	$\sigma_u$	$7.6 \times 10^{-3}$	m
L2 Field Width Constant	$\sigma_{L2}$	$0.373 \times 10^{-6}$	s
Detuning Between the Ground States	$\Delta$	$(4 \times 10^3 \times 2\pi)$	rad/s
2nd depletion laser Detuning	$\delta_{L2}$	$(3 \times 10^6 \times 2\pi)$	rad/s

Table 2.1: Table of Experiment Parameters and Constants. Values in bracket are the maximum value set to the corresponding variable.

Figure (2.2) presents examples of simulated asymmetry  $\mathcal{A}$  versus energy detuning  $\Delta$  along with fits denoted as red curves.  $W, a_0$ , and  $a_1$  are extracted from the fitting as mentioned earlier, taking Eqn. (2.30) as the model. Notice the simulation data for  $|\Delta/(2\pi)| \leq 1\text{MHz}$  are ignored during fitting.

We performed numerical simulations by directly incorporating constants from the experimental setup into the Schrödinger equation without any modifications. However, the resulting data showed significant discrepancies from the experimental observations. Specifically, while the simulated values of  $W, a_0$ , and  $a_1$  exhibit a linear dependence on the non-reversing field strength  $\mathcal{E}_{\text{nr},0}$ , consistent with experiment result, the slope  $S \equiv W/\mathcal{E}_{\text{nr}}$  did not show the expected linear dependence on the 2nd depletion laser detuning  $\delta_{L2}$ , as reported in previous experiments. Instead, the slope displayed oscillatory behavior with respect to  $\delta_{L2}$ . More notably, the magnitude of  $W$  and related quantities was approximately two orders of

magnitude smaller than the experimental values.

To reproduce the experimental results, we then systematically varied parameters that could reasonably deviate from their nominal values in the actual setup. These included the 2nd depletion laser intensity, the L2 field envelope width  $\sigma_{L2}$ , the center position of the non-reversing field  $t_{nr}$ , and the molecular beam velocity  $v$ . Among these, only reducing the 2nd depletion laser strength to approximately 9% of its theoretical value—calculated based on an 8 mW laser power—enabled the simulation to closely reproduce the experimental results. Adjusting the other parameters did not yield comparable agreement.

Additionally, previous measurements of the 2nd depletion laser’s optical pumping ratio (OPR) near zero detuning showed values around 8–9% (a low OPR—indicating high depletion efficiency is critical for this experiment), which might caused by the so-called “rain-down effect,” where spontaneous decay from higher-lying states populated during the ablation stage leads to a residual background population in the even-parity state. As shown in Figure 7.8 of Emine’s thesis, the OPR increases rapidly with detuning away from resonance, suggesting that the depletion laser was not sufficiently strong to fully saturate the transition. In fact, numerical simulations of OPR as a function of laser intensity further support this interpretation. If the laser were operating at the nominal 8 mW, the OPR would remain largely flat with detuning. However, when the intensity was reduced to approximately 15% of the theoretical value, the simulated OPR vs. detuning curve closely matched experimental data, aside from a constant offset likely due to the background that the simulation doesn’t take into account. This result, together with the requirement to reduce the 2nd depletion laser field strength to around 10% in order to reproduce both the error signal and OPR behavior, strongly suggest that the actual laser intensity in the experiment was significantly lower than the expected 8 mW, such that the effective laser intensity is likely closer to 10% of that value. Figure (2.3) shows the result from those fitting with reduced laser intensity.

(maybe? figure for  $\delta_{L2}$  vs. OPR at different intensity... )

To further investigate the origin of the observed systematic error, we employed numerical

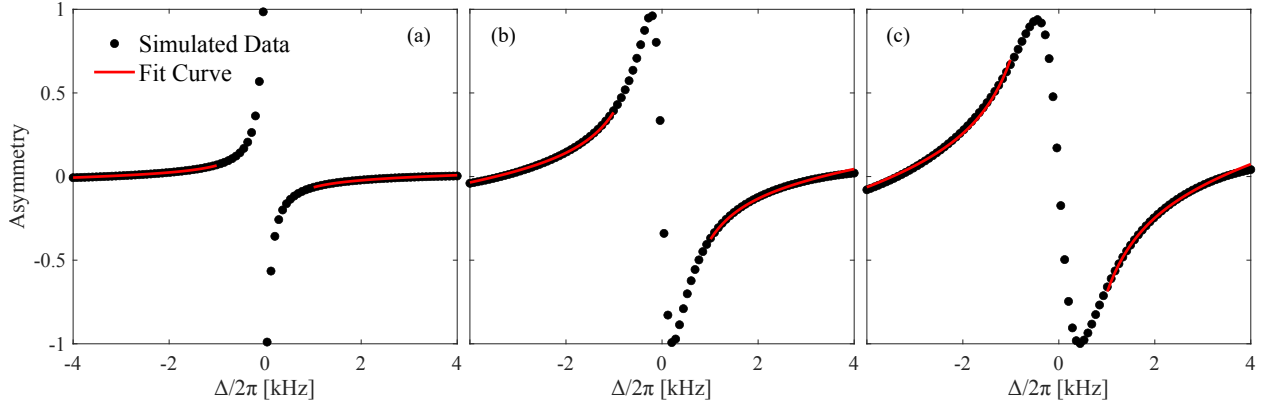


Figure 2.2: Examples of simulated asymmetry data (black) and fits (red) taking Eqn. (2.30) as the model. Simulations are generated using the electric field defined in Eqn. (2.4)-Eqn. (2.6). The input parameters are listed in Table (2.1), except the 2nd depletion laser field strength is set to 9% of the theoretical value, which is  $\mathcal{E}_{L2,0} \approx 108.4$  V/m, and the non-reversing field strength  $\mathcal{E}_{nr,0}$  are (a) 1 V/m, (b) 6 V/m, (c) 12 V/m.

simulations to systematically study the sensitivity of this effect to various experimental parameters. We first analyzed the dependence of the systematic shift on the positioning of the non-reversing field and the 2nd depletion laser. Then, we examined the influence of temporal variations in the non-reversing field in the vicinity of the L2 pulse. Finally, we assessed which temporal segment of the non-reversing field, relative to the 2nd depletion laser, contributes most significantly to the systematic effect. These analyses will help our understanding of this systematic error and provide guidance for the theoretical calculation presented in the following sections.

As the simulation reproduces the experimental error signals only when the laser intensity is reduced to approximately 9% of its nominal theoretical value at 8 mW, we will, unless otherwise specified, adopt a reduced L2 field strength of  $\mathcal{E}_{L2,0} = 9\% \times 1204.1$  V/m = 108.4 V/m throughout the remainder of this chapter to analyze the effect. For the rest of the section, we will only present the simulation result for  $W$  extracted with  $\mathcal{E}_{nr,0} = 12$  V/m and  $\delta_{L2} = 2\pi \times 3$  MHz to represent the effect of changing parameters.

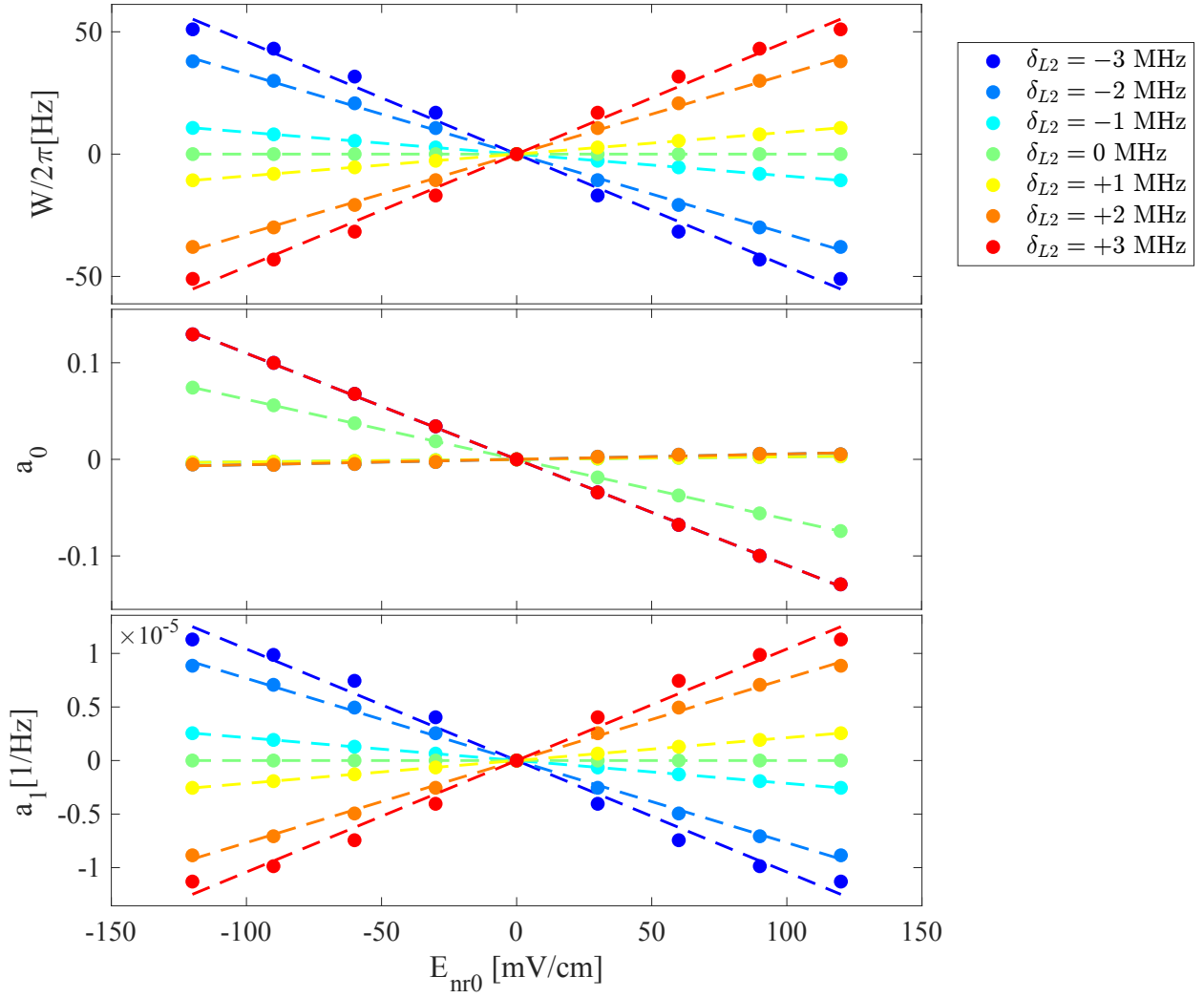


Figure 2.3: Reproduction of the systematic error search measurements (Emine's thesis Figure (7.9)) using simulation, made with an intentionally amplified unipolar  $\mathcal{E}_{nr}$  pulse centered at Gap 22 and a deliberate laser detuning in 2nd depletion laser,  $\delta_{L2}$ , with a reduced strength  $\mathcal{E}_{L2,0} = 108.4$  V/m. Fit results are calculated by fitting the asymmetry signal to Eqn. (2.30). Lines are fit to the data with the model function  $f(x) = mx+b$ , where  $m, b$  are fit parameters. Data and the best fit lines are color matched.

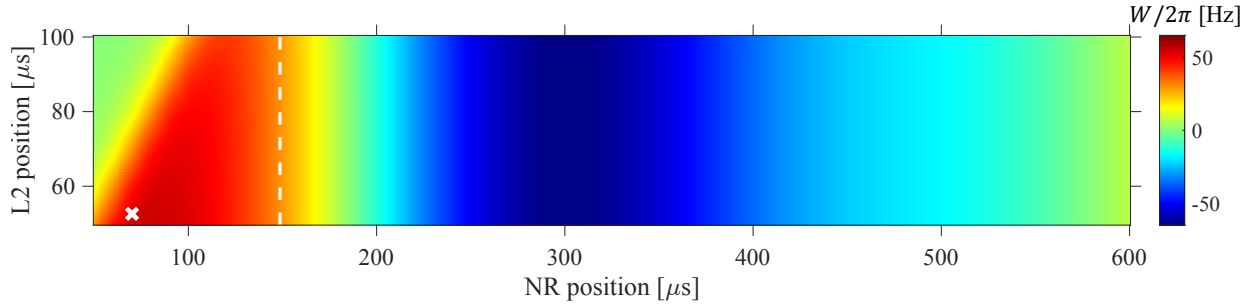


Figure 2.4: Simulated map of  $W$  as function of the center position of the 2nd depletion laser and the original non-reversing field  $\mathcal{E}_{\text{nr}}$ . The white cross indicates the actual fields position in the apparatus and the white dotted line represents the end of the interaction region in experiment. All the simulations are conducted with  $\mathcal{E}_{\text{nr},0} = 12 \text{ V/m}$  and  $\delta_{L2} = 2\pi \times 3 \text{ MHz}$ , started from  $t_{L1} = -51.1 \mu\text{s}$  and obtained the even parity ground state amplitude  $c_-$  at  $t = 700 \mu\text{s}$ .

### Dependence of $W$ on $\mathcal{E}_{\text{nr}}$ and $\mathcal{E}_{L2}$ Field Positions

Previous experimental studies have indicated that a significant systematic shift in  $W$  arises only when the non-reversing field  $\mathcal{E}_{\text{nr}}$  is positioned near the second depletion laser L2, specifically, in the vicinity of Gap 22. However, due to constraints imposed by the geometry of the experimental apparatus, it was not feasible to continuously scan the position of  $\mathcal{E}_{\text{nr}}$  to determine its precise relationship with the systematic error. In contrast, numerical simulations are not subject to such limitations. The position of  $\mathcal{E}_{\text{nr}}$  can be freely varied, even goes to the regions far beyond the physical bounds of the interaction region in the experiment. This flexibility enables us to construct a detailed spatial map of the induced shift in  $W$  as a function of the position of  $\mathcal{E}_{\text{nr}}$ . Additionally, we simultaneously varied the position of the 2nd depletion laser field  $\mathcal{E}_{L2}$  to explore the influence of the relative position between fields on the systematic error.

Figure (2.4) presents a two-dimensional position map showing the variation of  $W$  as a function of the spatial positions of both  $\mathcal{E}_{\text{nr}}$  and  $\mathcal{E}_{L2}$ . All the simulation results are started from  $t_{L1} = -51.1 \mu\text{s}$  and extract the even parity ground states amplitude at  $t = 700 \mu\text{s}$  so all the non-trivial part of  $\mathcal{E}_{\text{nr}}$  is included.

The position map shows that a nonzero value of  $W$  emerges only when the non-reversing

field  $\mathcal{E}_{\text{nr}}$  is located at or after the position of the 2nd depletion laser  $\mathcal{E}_{L2}$ . Consistent with experimental observations, the shift  $W$  reaches a minimum (corresponding to maximum amplitude) when  $\mathcal{E}_{\text{nr}}$  is positioned immediately after  $\mathcal{E}_{L2}$ . As  $\mathcal{E}_{\text{nr}}$  is moved further downstream,  $W$  gradually increases toward zero. Interestingly, when  $\mathcal{E}_{\text{nr}}$  is placed even further downstream, beyond the boundaries of the apparatus,  $W$  begins to rise again, reaching a maximum of comparable magnitude to the earlier minimum but with opposite sign, before eventually returning to zero and crossing into negative values once more. This oscillatory behavior strongly suggests that the systematic effect is not purely a local phenomenon arising from a direct interaction between  $\mathcal{E}_{\text{nr}}$  and  $\mathcal{E}_{L2}$ , as previously hypothesized. Rather, the observation that  $W$  continues to vary even when  $\mathcal{E}_{\text{nr}}$  is positioned far from  $\mathcal{E}_{L2}$  indicates the presence of interference effects, likely arising from different phase of the molecular wavefunction when it sees the  $\mathcal{E}_{\text{nr}}$  due to different free precession duration.

### Dependence of $W$ on Variations of $\mathcal{E}_{\text{nr}}$ Near the 2nd depletion laser $\mathcal{E}_{L2}$

Previous section shows that the observed systematic shift in  $W$  is not solely due to a local interaction between the non-reversing field  $\mathcal{E}_{\text{nr}}$  and the second depletion laser  $\mathcal{E}_{L2}$ , it remains unclear whether the pronounced value of  $|W|$  observed when  $\mathcal{E}_{\text{nr}}$  is positioned immediately after  $\mathcal{E}_{L2}$  is the result of such an interaction. This uncertainty arises in part because  $\mathcal{E}_{\text{nr}}$  exhibits the steepest variation in this spatial region. In this part, we aim to investigate whether the time-domain gradient of  $\mathcal{E}_{\text{nr}}$  in the vicinity of  $\mathcal{E}_{L2}$  plays a meaningful role in producing the systematic effect.

We compare the simulated values of  $W$  obtained using the original  $\mathcal{E}_{\text{nr}}(t)$  and a modified version  $\mathcal{E}_{\text{nr}}^{\text{MOD}}(t)$  (Figure (2.5)), in which the field has been flattened in time around the center of the 2nd depletion laser. This modified field is defined as:

$$\mathcal{E}_{\text{nr}}^{\text{MOD}}(t) = M(t) \cdot \mathcal{E}_{\text{nr}}(t_{L2}) + (M(t) - 1) \cdot \mathcal{E}_{\text{nr}}(t) \quad (2.31)$$

where  $M(t)$  is a smooth masking function designed to transition gradually between the

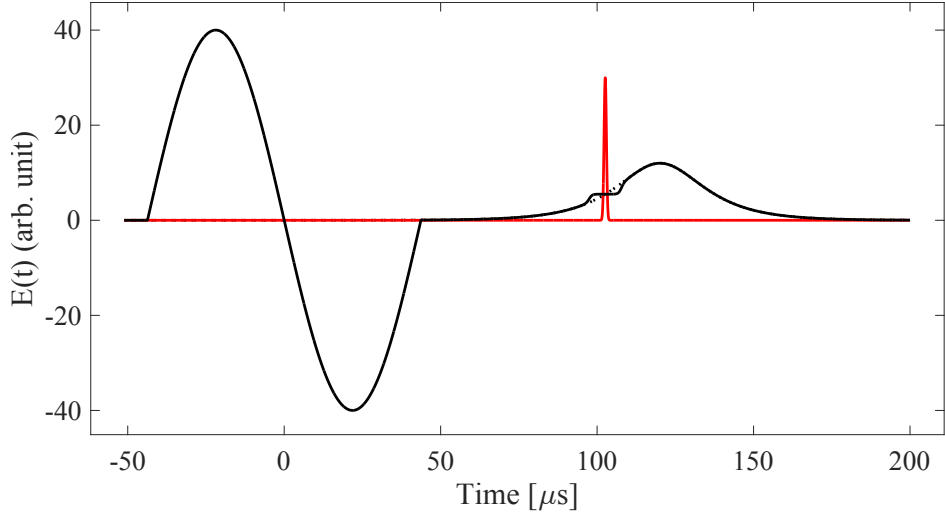


Figure 2.5: Modified non-reversing field  $\mathcal{E}_{\text{nr}}^{\text{MOD}}$ , as defined in Eqn. (2.31). A smooth mask function  $M(t)$  is used to eliminate any time dependency of  $\mathcal{E}_{\text{nr}}$  around the center of the 2nd laser pulse ( $t_{L2}$ ). The solid black curve shows the sum of  $\mathcal{E}_{\text{stark}}$  and  $\mathcal{E}_{\text{nr}}^{\text{MOD}}$ . The dotted black lines indicates the original  $\mathcal{E}_{\text{nr}}$ , while the red curve represents the time-dependent envelope of the 2nd depletion laser strength,  $\mathcal{E}_{L2,0}$ . All curves are shown in arbitrary units and are not to scale.

flattened and unmodified regions, thereby avoiding artificial sharp edges. The mask function is given by:

$$M(t) = \frac{1}{4} \left[ 1 + \tanh \left( \frac{t - t_{L2} + 5 \mu\text{s}}{1 \mu\text{s}} \right) \right] \left[ 1 + \tanh \left( \frac{t_{L2} - t + 5 \mu\text{s}}{1 \mu\text{s}} \right) \right] \quad (2.32)$$

This function smoothly interpolates a plateau of width approximately  $10 \mu\text{s}$  centered at  $t_{L2}$ , suppressing any rapid changes in the field around  $\mathcal{E}_{L2}$ . The constant offset in  $\mathcal{E}_{\text{nr}}$  near the L2 pulse shouldn't be the cause of this effect, as a uniform static field during the application of  $\mathcal{E}_{L2}$  would contribute only a small DC Stark shift, which is negligible for our purposes.

Figure (2.6) presents a comparison between the simulated  $W$  values obtained using the original and modified non-reversing fields. The results show that, the variation of  $\mathcal{E}_{\text{nr}}$  in the immediate vicinity of  $\mathcal{E}_{L2}$  does not significantly contribute to the systematic shift in  $W$ . This suggests that the dominant mechanism responsible for the observed effect is not local in nature but instead likely arises from interference phenomena, as we discussed earlier.

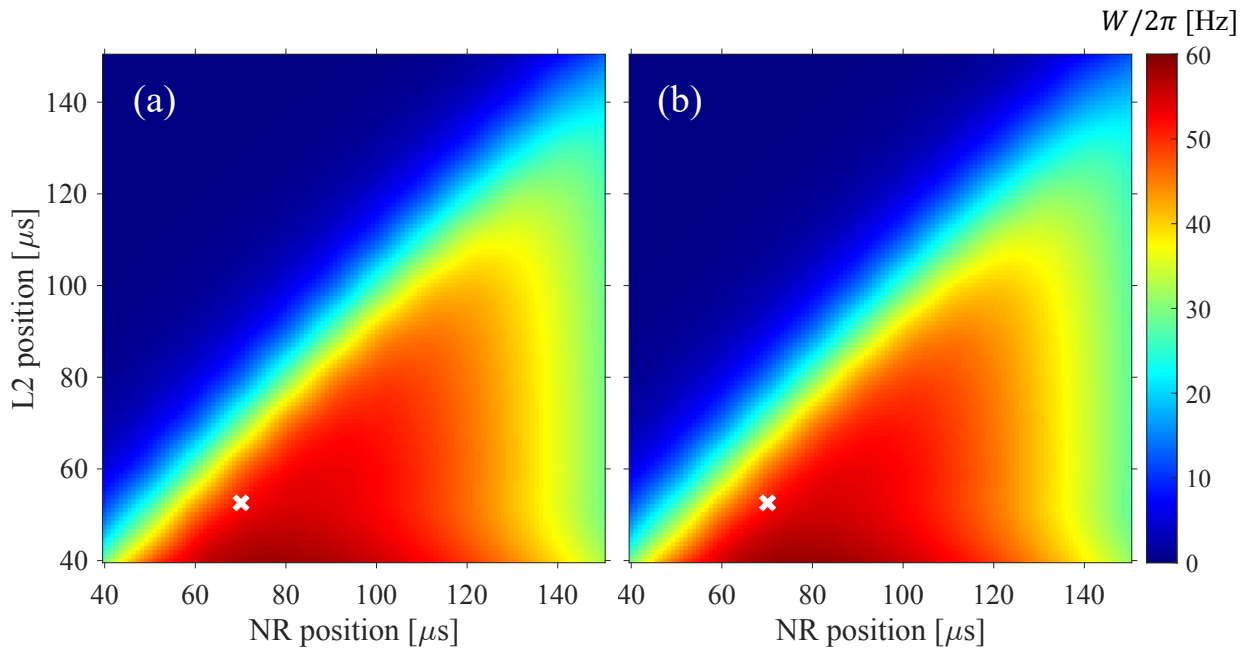


Figure 2.6: Comparison of simulated maps of  $W$  with  $\mathcal{E}_{\text{nr}}$  and  $\mathcal{E}_{\text{nr}}^{\text{MOD}}$ , as function of the center position of the 2nd depletion laser and the non-reversing field. (a) shows the result with the original  $\mathcal{E}_{\text{nr}}$ , and (b) shows the result with the  $\mathcal{E}_{\text{nr}}^{\text{MOD}}$  defined in Eqn. (2.31). The white cross indicates the actual fields position in the apparatus. The near-equivalence of the two maps supports the conclusion that the detailed shape of  $\mathcal{E}_{\text{nr}}$  near the 2nd laser does not significantly contribute to the observed shift in  $W$ . All the simulations are conducted with  $\mathcal{E}_{\text{nr},0} = 12 \text{ V/m}$  and  $\delta_{L2} = 2\pi \times 3 \text{ MHz}$ .

## Dependence of $W$ on $\mathcal{E}_{\text{nr}}$ Before and After the 2nd Depletion Laser

The fact that parameter  $W$  is nonzero only when  $\mathcal{E}_{\text{nr}}$  is present at or after  $\mathcal{E}_{\text{L2}}$ , suggests that the portion of  $\mathcal{E}_{\text{nr}}$  occurring prior to the 2nd depletion laser does not contribute meaningfully to the resulting shift in  $W$ . Consequently, it appears justified to neglect  $\mathcal{E}_{\text{nr}}$  before the L2 region in the construction of an analytic model for  $W$ . To rigorously test this hypothesis, we performed a comparative numerical analysis across three distinct scenarios:

1. The original field profile, corresponding to the unmodified  $\mathcal{E}_{\text{nr}}(t)$  as used in the experiment;
2. A modified profile  $\mathcal{E}_{\text{nr}}^{\text{after L2}}(t)$  where  $\mathcal{E}_{\text{nr}}$  is set to zero before the 2nd depletion laser;
3. A modified profile  $\mathcal{E}_{\text{nr}}^{\text{before L2}}(t)$  where  $\mathcal{E}_{\text{nr}}$  is set to zero after the 2nd depletion laser.

To implement the latter two modifications smoothly and avoid artifacts due to discontinuities, we introduced hyperbolic tangent cutoffs around  $t_{\text{L2}}$  like before. The field profiles in these cases are defined as:

$$\mathcal{E}_{\text{nr}}^{\text{before L2}}(t) = \mathcal{E}_{\text{nr}}(t) \cdot \frac{1}{2} \left[ 1 + \tanh \left( \frac{t_{\text{L2}} - t}{1 \mu\text{s}} \right) \right] \quad (2.33)$$

$$\mathcal{E}_{\text{nr}}^{\text{after L2}}(t) = \mathcal{E}_{\text{nr}}(t) \cdot \frac{1}{2} \left[ 1 + \tanh \left( \frac{t - t_{\text{L2}}}{1 \mu\text{s}} \right) \right] \quad (2.34)$$

Figure (2.7) illustrates those three field configurations and Figure (2.8) shows the resulting  $W$  maps under these three configurations. It is evident that the output using  $\mathcal{E}_{\text{nr}}^{\text{before L2}}(t)$  closely resembles that of the original unmodified field. In contrast, the case using  $\mathcal{E}_{\text{nr}}^{\text{after L2}}(t)$  yields a null result for  $W$ , indicating that contributions to  $W$  originate exclusively from the region of  $\mathcal{E}_{\text{nr}}$  located after the L2 interaction zone. This result allows us to ignore any residual non-reversing field before 2nd depletion laser, thereby simplifying the analytic treatment of  $W$  presented later.

The simulation results presented above clearly demonstrate that a systematic shift in  $W$  is only observed when the non-reversing electric field  $\mathcal{E}_{\text{nr}}$  is located *after* the position of the

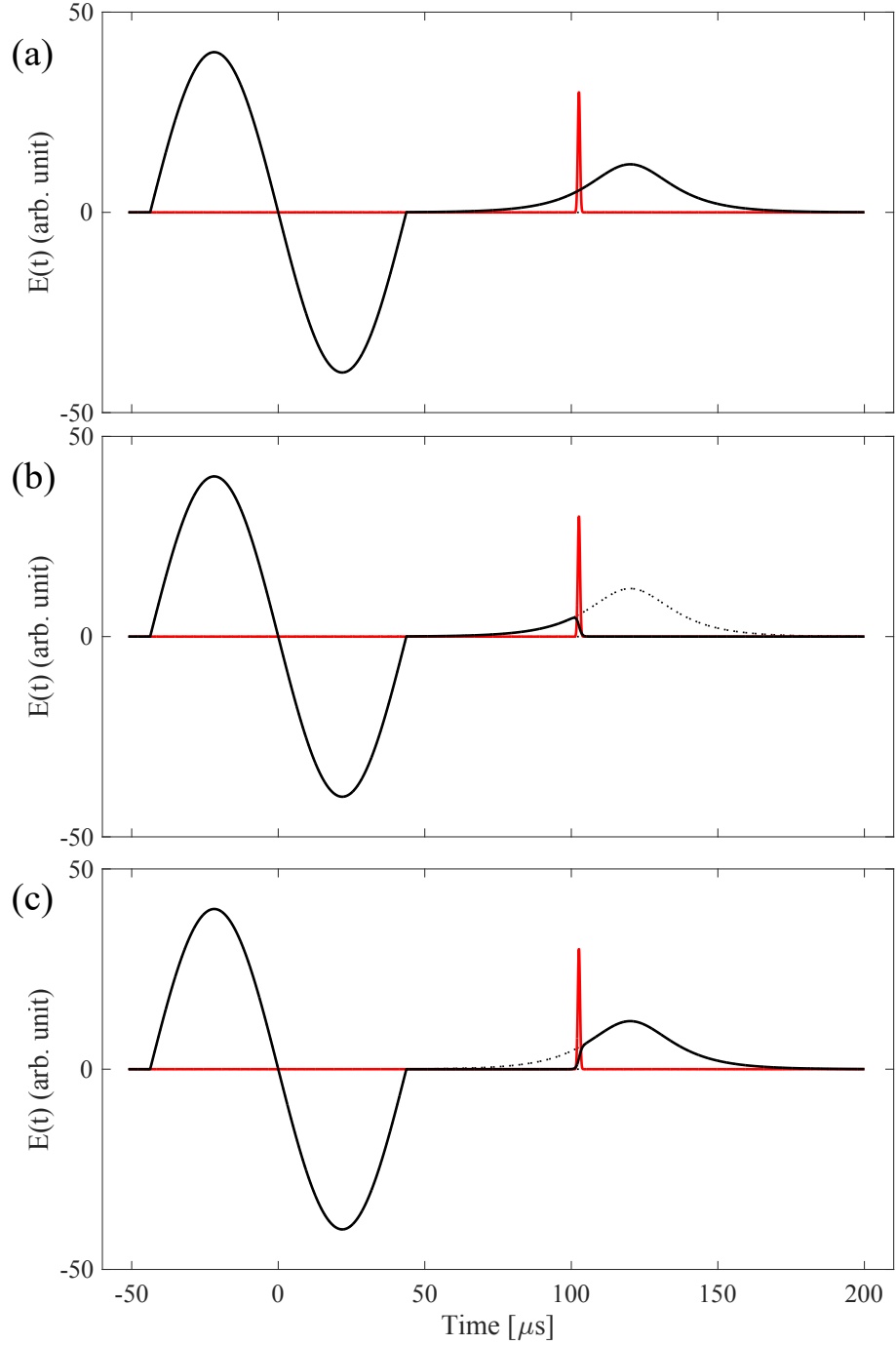


Figure 2.7: Illustrations of the total field with (a) the original non-reversing field  $\mathcal{E}_{\text{nr}}$ , (b) the non-reversing field before 2nd depletion laser  $\mathcal{E}_{\text{nr}}^{\text{before } \text{L}2}$ , and (c) the non-reversing field after 2nd depletion laser  $\mathcal{E}_{\text{nr}}^{\text{after } \text{L}2}$ , as defined in Eqn. (2.33) and Eqn. (2.34). A smooth mask function is used to eliminate the  $\mathcal{E}_{\text{nr}}$  before and after the center of the 2nd laser pulse ( $t_{\text{L}2}$ ). The solid black curves are the sum of  $\mathcal{E}_{\text{stark}}$  and respective modified non-reversing field. The original  $\mathcal{E}_{\text{nr}}$  profile is overlay on top as dotted black lines, while the red curve represents the time-dependent envelope of the 2nd depletion laser strength,  $\mathcal{E}_{\text{L}2,0}$ . All curves are shown in arbitrary units and are not to scale.

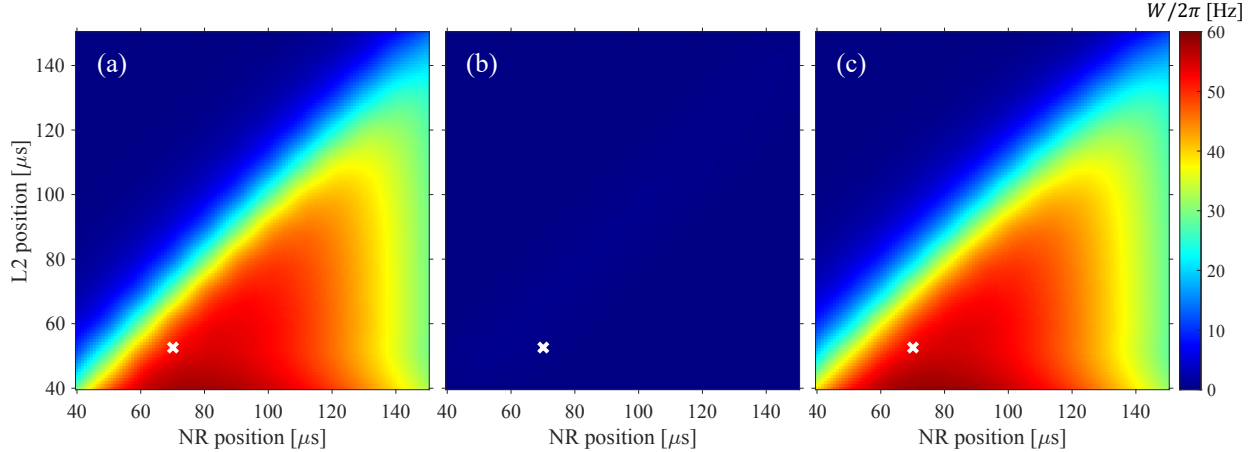


Figure 2.8: Comparison of simulated maps of  $W$  with (a) the original non-reversing field  $\mathcal{E}_{\text{nr}}$ , (b) the non-reversing field before 2nd depletion laser  $\mathcal{E}_{\text{nr}}^{\text{before } \mathcal{L}^2}$ , and (c) non-reversing field after 2nd depletion laser  $\mathcal{E}_{\text{nr}}^{\text{after } \mathcal{L}^2}$ , as function of the center position of the 2nd depletion laser and the non-reversing field. The white cross indicates the actual fields position in the apparatus. All the simulations are conducted with  $\mathcal{E}_{\text{nr},0} = 12 \text{ V/m}$  and  $\delta_{L2} = 2\pi \times 3 \text{ MHz}$ .

2nd depletion laser  $\mathcal{E}_{L2}$ . Moreover, the spatial proximity between  $\mathcal{E}_{\text{nr}}$  and  $\mathcal{E}_{L2}$  is not critical:  $\mathcal{E}_{\text{nr}}$  may be positioned significantly downstream without diminishing its effect on  $W$ . In contrast, any residual field present before or even coincident with  $\mathcal{E}_{L2}$  does not contribute meaningfully to the observed shift and can therefore be safely neglected.

Those numerical simulation results allows a powerful simplification. The experimental configuration can be treated as three spatially and dynamically distinct regions, each dominated by a separate field:  $\mathcal{E}_{\text{stark}}$ ,  $\mathcal{E}_{L2}$ ,  $\mathcal{E}_{\text{nr}}$ . These regions are effectively non-overlapping and mutually independent. This separation allows us to model each region in isolation using simplified two-level systems, with appropriate initial conditions inherited from the preceding stage. In particular, the evolution within each region can be captured analytically by treating only the relevant two states coupled by the field in question. We will leverage this simplified framework in the following section to construct an analytic model for the system dynamics, which will finally bring us the approximated expressions for the error signal  $W$ ,  $a_0$ , and  $a_1$ .

## 2.2.2 Analytical Model with a Gaussian $\mathcal{E}_{\text{nr}}$ Pulse and Imperfection

The simulation presents in the previous section shows that we can treat  $\mathcal{E}_{\text{stark}}$ ,  $\mathcal{E}_{L2}$ ,  $\mathcal{E}_{\text{nr}}$  as three fields that act independently to the molecule beam in sequence. Since each field would only couple to two of the states in our system, the evolution within each region can be captured analytically by treating only the relevant two states coupled by the field in that section, and appropriate the final state as the initial condition for the next stage. Figure (2.9) illustrates the simplified model with yellow dotted vertical lines denotes the separations of different sections. Although in the simplified model the entire process is divided into three regions of approximately equal size, as depicted in Figure (2.9), in the following derivation, for convenience, we approximate the duration of Region 2 and the second depletion laser pulse as zero when solving the system dynamics in Region 1 and Region 3, with the center of the second depletion laser aligned with the endpoint of Region 1 and the starting point of Region 3. In contrast, when calculating the dynamics within Region 2, we retain the original full time-domain profile of the second depletion laser as defined in Eqn. (2.6). In this section, an analytic model for the system dynamics is derived using this simplification, then, an expression for asymmetry  $\mathcal{A}_{\text{analytic}}(\Delta)$  is derived. Finally, we map this asymmetry function to the fitting function Eqn. (2.30) to obtain an analytic expression for  $W$ ,  $a_0$ , and  $a_1$ .

### Region 1: Stark Field

We begin by solving Region 1, where the only active interaction is the Stark field  $\mathcal{E}_{\text{stark}}$ . To make things easier, we redefine the time axis of the dynamics to begin at  $t = 0$ , the start of the Stark field, and stops at  $t = T_e$ . Any free precession occurring during the field-free evolution intervals  $T_{f1}$  and  $T_{f2}$  will be incorporated afterward simply as a phase factor.

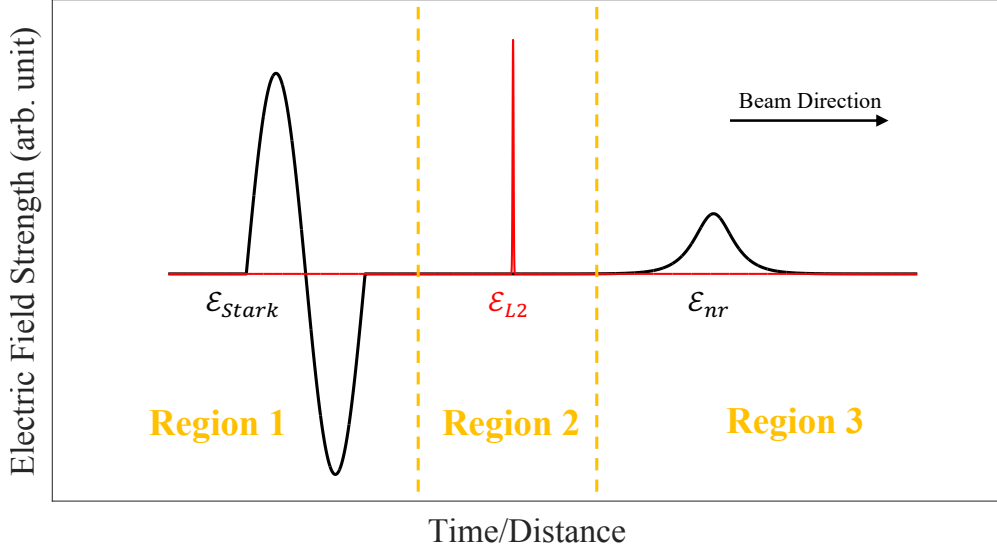


Figure 2.9: Illustration of three independent fields model

Recall the equivalent non-Hermitian Hamiltonian for our three level system reads:

$$\mathcal{H}_N = \begin{pmatrix} 0 & \Omega_{12}(t) & 0 \\ \Omega_{12}(t) & \Delta & \frac{1}{2}\Omega_{13}(t) \\ 0 & \frac{1}{2}\Omega_{13}(t) & \delta_{L2} - i\frac{\Gamma}{2} \end{pmatrix} \quad (2.35)$$

The system in Region 1 can be approximated by a two-level subsystem consisting of two opposite parity ground states. The relevant Hamiltonian in this subspace is obtained by truncating the full non-Hermitian three-level Hamiltonian by omitting the third state which is far off-resonance in this region. The effective two-level Hamiltonian in the parity basis  $\{|\psi^+\rangle, |\psi^-\rangle\}$  reads:

$$\mathcal{H}_1(t) = \begin{pmatrix} 0 & \Omega_{12}(t) \\ \Omega_{12}(t) & \Delta \end{pmatrix} \quad (2.36)$$

where  $\Delta$  is the detuning between the parity eigenstates and  $\Omega_{12}(t) = d_{12} \cdot \mathcal{E}_{\text{stark}}(t)$  is the time-dependent Rabi coupling induced by the Stark field. We write the wavefunction in the

rotating frame of the upper (odd-parity) state:

$$|\Psi_{12}(t)\rangle = c_+(t)|\psi^+\rangle + e^{-i\Delta_1 t}c_-(t)|\psi^-\rangle \equiv \begin{pmatrix} c_+(t) \\ e^{-i\Delta t}c_-(t) \end{pmatrix} \quad (2.37)$$

where the even and odd parity states  $|\psi^+\rangle = \begin{pmatrix} 1 \\ 0 \end{pmatrix}$  and  $|\psi^-\rangle = \begin{pmatrix} 0 \\ 1 \end{pmatrix}$  respectively. The time-dependent Schrödinger equations governing the evolution,  $H|\psi(t)\rangle = i\partial_t|\psi(t)\rangle$ , gives

$$\dot{c}_+(t) = -i e^{-i\Delta t} (d_{12} \cdot \mathcal{E}_{\text{stark}}) c_-(t) \quad (2.38)$$

$$\dot{c}_-(t) = -i e^{+i\Delta t} (d_{12} \cdot \mathcal{E}_{\text{stark}}) c_+(t) \quad (2.39)$$

Assuming the system is initially in the odd parity state, we set the initial condition  $c_+(0) = 0$ ,  $c_-(0) = 1$ , we solve this system using time-dependent perturbation theory (TDPT). At zeroth order, the coefficients remain unchanged

$$c_+^{(0)}(t) = 0, c_-^{(0)}(t) = 1 \quad (2.40)$$

where the superscript in parentheses indicates the order of approximation we included up to (i.e.  $c_+^{(2)}$  represents the even parity state amplitude calculated up to the second order). To calculate the first-order approximation, we insert the zeroth-order values into Eqns. (2.38)-(2.39) and get,

$$\dot{c}_+^{(1)}(t) = -ie^{-i\Delta t} d_{12} \cdot \mathcal{E}_{\text{stark}} \quad (2.41)$$

$$\dot{c}_-^{(1)}(t) = 0 \quad (2.42)$$

Now we integrate both sides from  $t = 0$  to  $t = T_e$ . For odd parity state, we have  $c_-^{(1)}(T_e) = 1$ .

For a sinusoidal Stark field given in Eqn. (2.4), we integrate and get

$$\begin{aligned}
c_+^{(1)}(T_e) &= \int_0^{T_e} \dot{c}_+^{(1)}(t') dt' = -id_{12}\mathcal{E}_0 \int_0^{T_e} e^{-i\Delta t'} \sin(\omega t') dt' \\
&= \frac{d_{12}\mathcal{E}_0 e^{-i\Delta T_e}}{\omega^2 - \Delta^2} [-\Delta \sin(\omega T_e) + i\omega \cos(\omega T_e) - i\omega e^{i\Delta T_e}] \\
&= -\frac{i\omega d_{12}\mathcal{E}_0 e^{-i\Delta T_e}}{\omega^2 - \Delta^2} [e^{i\Delta T_e} - 1] \\
&= \frac{2\omega d_{12}\mathcal{E}_0 e^{-i\Delta T_e/2}}{\omega^2 - \Delta^2} \sin(\Delta T_e/2)
\end{aligned}$$

Since this is the first region the system interacts with, any inaccuracies arising from the first-order TDPT approximation may amplify as the dynamics evolve through subsequent regions. To mitigate potential errors, we compute the second-order TDPT correction. The second order result for even parity state is trivial,  $c_+^{(2)}(T_e) = c_+^{(1)}(T_e)$ . Using Mathematica, the 2nd order TDPT result reads

$$c_+^{(2)}(T_e) = \frac{2\omega d_{12}\mathcal{E}_0 e^{-i\Delta T_e/2}}{\omega^2 - \Delta^2} \sin(\Delta T_e/2) \quad (2.43)$$

$$c_-^{(2)}(T_e) = 1 + \frac{d_{12}^2 \mathcal{E}_0^2 \left( (e^{iT_e\Delta} - 1)\omega^3 - i\pi(\Delta^3 - \Delta\omega^2) \right)}{\omega(\Delta^2 - \omega^2)^2} \quad (2.44)$$

To return to the lab frame, we must account for free evolution during the intervals  $T_{f1}$ ,  $T_e$ , and  $T_{f2}$ , which introduce an accumulated phase of  $e^{-i\Delta(T_{f1}+T_e+T_{f2})}$  on the odd-parity state.

Substituting back into Eqn. (2.37), the final state at  $t = t_{L2}$  is thus

$$|\Psi_{12}(t = t_{L2})\rangle = \left( \begin{array}{l} \frac{2\omega d_{12}\mathcal{E}_0 e^{-i\Delta T_e/2}}{\omega^2 - \Delta^2} \sin(\Delta T_e/2) \\ e^{-i\Delta\mathcal{T}} \left( 1 + \frac{d_{12}^2 \mathcal{E}_0^2}{\omega(\Delta^2 - \omega^2)^2} \left( (e^{iT_e\Delta} - 1)\omega^3 - i\pi(\Delta^3 - \Delta\omega^2) \right) \right) \end{array} \right) \quad (2.45)$$

where  $\mathcal{T} \equiv T_e + T_{f1} + T_{f2}$ . This result will serve as the initial condition for the next interaction region.

## Region 2: 2nd depletion laser

We now consider the system dynamics in Region 2, where the only active interaction is the 2nd depletion laser. The laser couples the odd-parity ground state  $|\psi^-\rangle$  to the even-parity excited state  $|\psi_e\rangle$ , while the even ground state  $|\psi^+\rangle$  remains uncoupled. Thus, the system can be effectively described by a two-level subsystem spanned by  $\{|\psi^-\rangle, |\psi_e\rangle\}$ . The effective non-Hermitian Hamiltonian in this basis is given by

$$\mathcal{H}_2(t) = \begin{pmatrix} \Delta & \frac{1}{2}\Omega_{13}(t) \\ \frac{1}{2}\Omega_{13}(t) & \delta_{L2} - i\frac{\Gamma}{2} \end{pmatrix} \approx \begin{pmatrix} 0 & \Omega'_{13}(t) \\ \Omega'_{13}(t) & z \end{pmatrix}, \quad (2.46)$$

where we have defined  $z \equiv \delta_{L2} - i\Gamma/2$  and absorbed a factor of  $1/2$  into the coupling:  $\Omega'_{13}(t) = \frac{1}{2}\Omega_{13}(t) = \frac{1}{2}d_{13}\mathcal{E}_{L2,0}(t)e^{-\frac{(t-t_{\text{diff}})^2}{2\sigma_{L2}^2}}$ . In second equation above, we have moved into the rotating frame where the approximation  $\Delta \ll \delta_{L2}$  was used. Because the 2nd depletion laser field is strong and not perturbative, we adopt the adiabatic approximation rather than first order TDPT. Assuming that the system is initially in the odd-parity state and follows the instantaneous eigenstate of the Hamiltonian adiabatically, the time-evolved wavefunction is

$$|\Psi_{23}(t)\rangle = e^{i\gamma(t)}e^{-i\Phi_{\text{dyn}}(t)} \begin{pmatrix} e^{-i\Delta t}c_-^{(2)}(t_{L2}) \\ c_e(t_{L2}) \end{pmatrix} \quad (2.47)$$

Here,  $\gamma(t)$  is the Berry (geometric) phase and  $\Phi_{\text{dyn}}(t)$  is the dynamical phase. In our case, only a single parameter (field amplitude) varies along a straight path in parameter space, so the trajectory encloses no area in parameter space, implying  $\gamma(t) = 0$ . The dynamical phase is given by the time integral of the eigenvalue associated with the adiabatically followed eigenstate. Since the initial state is odd parity, we follow the lower eigenvalue branch:

$$\Phi_{\text{dyn}}(t) = \int_0^t \lambda_-(t') dt' \quad (2.48)$$

where

$$\lambda_{\pm}(t) = \frac{1}{2} \left( z \pm \sqrt{z^2 + 4\Omega'_{13}(t)^2} \right). \quad (2.49)$$

Note that our non-Hermitian Hamiltonian has complex eigenvalues, which would give rise to a decay term. To analytically approximate the integral, we expand the square root using the binomial expansion:  $\sqrt{1+x} = \sum_{n=0}^{\infty} \binom{1/2}{n} x^n$ , where  $\binom{1/2}{n} = \frac{(1/2)(-1/2)(-3/2)\cdots(1/2-n+1)}{n!}$ . Applying this expansion yields

$$\sqrt{z^2 + 4\Omega'_{13}(t)^2} = z \sqrt{1 + \frac{4\Omega'_{13}(t)^2}{z^2}} = z \sum_{n=0}^{\infty} \binom{1/2}{n} \left( \frac{4\Omega'_{13}(t)^2}{z^2} \right)^n \quad (2.50)$$

Thus, the eigenvalue becomes

$$\lambda_{-}(t) = -\frac{z}{2} \sum_{n=1}^{\infty} \binom{1/2}{n} \left( \frac{4\Omega'_{13}(t)^2}{z^2} \right)^n \quad (2.51)$$

This expansion converges only when  $\left| \frac{4\Omega'_{13}(t)^2}{z^2} \right| < 1$ , which sets a constraint on the 2nd depletion laser field strength

$$\mathcal{E}_{L2,0} < \frac{|z|}{d_{13}} \approx \frac{|\delta_{L2} + i\Gamma/2|}{d_{13}} \approx 153 \text{ V/m} \quad (2.52)$$

or about 12.7% of the theoretical field strength corresponding to an 8 mW laser, using typical parameters listed in Table (2.1). Substituting Eqn. (2.51) into Eqn. (2.48) gives:

$$\begin{aligned} \Phi_{\text{dyn}}(t) &= \int_0^t \lambda_{-}(t') dt' \\ &= -\frac{1}{2} \sum_{n=1}^{\infty} \binom{1/2}{n} \frac{4^n}{z^{2n-1}} \int_0^t \Omega'_{13}(t')^{2n} dt' \\ &= -\frac{1}{2} \sum_{n=1}^{\infty} \binom{1/2}{n} \frac{4^n (d_{13} \mathcal{E}_{L2,0})^{2n}}{2^{2n} z^{2n-1}} \int_0^t e^{-\frac{n(t'-t_{\text{diff}})^2}{\sigma_{L2}^2}} dt' \\ &= -\frac{1}{2} \sum_{n=1}^{\infty} \binom{1/2}{n} \frac{(d_{13} \mathcal{E}_{L2,0})^{2n}}{z^{2n-1}} I_n \end{aligned}$$

Now, we evaluate the integral  $I_n$  by change of variables

$$u = \frac{\sqrt{n} (t' - t_{\text{diff}})}{\sigma_{L2}} \implies t' = t_{\text{diff}} + \frac{\sigma_{L2}}{\sqrt{n}} u \quad (2.53)$$

with  $dt' = \frac{\sigma_{L2}}{\sqrt{n}} du$ , the integral becomes

$$I_n = \frac{\sigma_{L2}}{\sqrt{n}} \int_{u_1}^{u_2} e^{-u^2} du \quad (2.54)$$

recall that  $\text{erf}(x) = \frac{2}{\sqrt{\pi}} \int_0^x e^{-u^2} du$ ,

$$\int_{u_1}^{u_2} e^{-u^2} du = \int_0^{u_2} e^{-u^2} du - \int_0^{u_1} e^{-u^2} du = \frac{\sqrt{\pi}}{2} [\text{erf}(u_2) - \text{erf}(u_1)] \quad (2.55)$$

substitute back in

$$I_n = \frac{\sigma_{L2}}{\sqrt{n}} \cdot \frac{\sqrt{\pi}}{2} [\text{erf}(u_2) - \text{erf}(u_1)] = \frac{\sigma_{L2}}{2} \sqrt{\frac{\pi}{n}} \left[ \text{erf}\left(\frac{\sqrt{n}(t - t_0)}{\sigma_{L2}}\right) - \text{erf}\left(\frac{-\sqrt{n}t_0}{\sigma_{L2}}\right) \right] \quad (2.56)$$

Assuming the laser pulse is fully contained within Region 2, i.e.,  $t_0 \gg \sigma_{L2}$  and  $t \gg t_0$  and use the fact that  $\text{erf}(\pm\infty) = \pm 1$  so that

$$I_n \approx \sigma_{L2} \sqrt{\frac{\pi}{n}}$$

Therefore, the accumulated dynamical phase simplifies to

$$\Phi_{\text{dyn}}(\infty) \approx - \sum_{n=1}^{\infty} \binom{1/2}{n} \sqrt{\frac{\pi}{n}} \frac{(d_{13} \mathcal{E}_{L2,0})^{2n} \sigma_{L2}}{2z^{2n-1}} \quad (2.57)$$

The amplitude of the odd-parity ground state after L2 becomes

$$\begin{aligned}
c_-^{(2,N)}(t \geq t_{L2}) &= c_-^{(2)}(t_{L2}) \exp(-i\Phi_{\text{dyn}}^{(N)}(\infty)) \\
&= \left( 1 + \frac{d_{12}^2 \mathcal{E}_0^2}{\omega(\Delta^2 - \omega^2)^2} \left( (e^{iT_e\Delta} - 1) \omega^3 - i\pi(\Delta^3 - \Delta\omega^2) \right) \right) \\
&\quad \times \exp \left( i \sum_{n=1}^N \binom{1/2}{n} \sqrt{\frac{\pi}{n}} \frac{(d_{13}\mathcal{E}_{L2,0})^{2n} \sigma_{L2}}{2z^{2n-1}} \right) \quad (2.58)
\end{aligned}$$

where the superscript  $(2, N)$  indicates a truncation at order  $N$  for the dynamical phase and second-order TDPT result from Region 1. Although the result is strictly valid only a few  $\sigma_{L2}$  after  $t_{L2}$ , for simplicity, we approximate it as valid for all  $t \geq t_{L2}$ , since we will set  $t = t_{L2}$  as the initial condition for the calculations in Region 3. Given that the excited state amplitude doesn't play a role in the error signal, also it is a short-lived state, we set  $c_e(t > t_{L2}) = 0$ . Note that when moving back to the lab frame, one have to multiply the accumulated phase  $e^{-i\Delta(t+\mathcal{T})}$  to this result.

### Region 3: Non-Reversing Field

We have obtained the analytic expression for  $c_-(t)$  and  $c_+(t)$  for the system after passing Region 1 and 2. Now we use this result as the initial condition to compute the system dynamics under non-reversing field perturbation again using first order TDPT. The equivalent two level Hamiltonian is of the same form as Eqn. (2.36), except the Rabi frequency in this region becomes  $\Omega_{12}(t) = d_{12} \cdot \mathcal{E}_{\text{nr}}(t)$ . For ease of calculation, the non-reversing field is approximated to

$$\begin{aligned}
\mathcal{E}_{\text{nr}}(t) &= \mathcal{E}_{\text{nr},0} \operatorname{sech} \left( \frac{v(t - t_{\text{nr}})}{\sigma_u} \right) \\
&\approx \mathcal{E}_{\text{nr},0} \exp \left( -\frac{1}{2\sqrt{2}} \left( \frac{v(t - t_{\text{nr}})}{\sigma_u} \right)^2 \right) \\
&\equiv \mathcal{E}_{\text{nr},0} \exp(-a(t - t_{\text{nr}})^2) \quad (2.59)
\end{aligned}$$

where  $a \equiv \frac{v^2}{2\sqrt{2}\sigma_u^2}$ . This approximation has been verified to produce no discernible difference in the results. Assume  $t_{\text{nr}} \gg t_{L2}$ . Consider general wavefunction in rotating frame with basis  $\{|\psi^+\rangle, |\psi^-\rangle\}$  defined as in Eqn. (2.37), solving the first order TDPT gives the amplitude of even parity state

$$\begin{aligned} c_+^{(1)}(\infty) &= c_+(t_{L2}) - ic_-(t_{L2})d_{12} \int_{t_{L2}}^{\infty} e^{-i\Delta t'} \mathcal{E}_{\text{nr}}(t') dt' \\ &= c_+(t_{L2}) - ic_-(t_{L2})d_{12} \mathcal{E}_{\text{nr},0} \int_{t_{L2}}^{\infty} e^{-i\Delta t'} e^{-a(t'-t_{\text{nr}})^2} dt' \\ &\approx c_+(t_{L2}) - ic_-(t_{L2}) \sqrt{\frac{\pi}{a}} d_{12} \mathcal{E}_{\text{nr},0} e^{-i\Delta t_{\text{diff}} - \Delta^2/4a} \end{aligned} \quad (2.60)$$

where  $t_{\text{diff}} \equiv t_{\text{nr}} - t_{L2}$  is the time difference between the non-reversing field and 2nd depletion laser.

### Piecing Everything Together

Now, we plug Eqn. (2.45) and Eqn. (2.58) into Eqn. (2.60) and get

$$\begin{aligned} c_+^{(2,N,1)}(\infty) &= \frac{2\omega d_{12} \mathcal{E}_0 e^{-i\Delta T_e/2}}{\omega^2 - \Delta^2} \sin(\Delta T_e/2) \\ &\quad - i \left( 1 + \frac{d_{12}^2 \mathcal{E}_0^2}{\omega(\Delta^2 - \omega^2)^2} \left( (e^{iT_e\Delta} - 1) \omega^3 - i\pi(\Delta^3 - \Delta\omega^2) \right) \right) \\ &\quad \times \exp \left( i \sum_{n=1}^N \binom{1/2}{n} \sqrt{\frac{\pi}{n}} \frac{(d_{13} \mathcal{E}_{L2,0})^{2n} \sigma_{L2}}{2z^{2n-1}} \right) d_{12} \mathcal{E}_{\text{nr},0} \sqrt{\frac{\pi}{a}} e^{-i\Delta(t_{\text{diff}} + \mathcal{T}) - \Delta^2/4a} \end{aligned} \quad (2.61)$$

Simplify the expression by assuming  $\omega \gg \Delta$ , and only take the first order approximation for the binomial expansion in Region 2,  $N = 1$ , we have

$$\begin{aligned} c_+^{(2,N=1,1)}(\infty) &\approx \frac{2d_{12}\mathcal{E}_0}{\omega} e^{-i\Delta T_e/2} \sin(\Delta T_e/2) \\ &\quad - i \left( 1 + \frac{d_{12}^2 \mathcal{E}_0^2}{\omega^2} (e^{iT_e\Delta} - 1) \right) \cdot \exp\left(\frac{i}{4} d_{13}^2 \mathcal{E}_{L2,0}^2 \sqrt{\pi} \sigma_{L2} \frac{1}{\delta_{L2} - i\frac{\Gamma}{2}}\right) \\ &\quad \times d_{12} \mathcal{E}_{nr,0} \sqrt{\frac{\pi}{a}} e^{-i\Delta(t_{diff}+\mathcal{T})-\Delta^2/4a} \end{aligned} \quad (2.62)$$

Define

$$\begin{aligned} K_1 &= \frac{2d_{12}\mathcal{E}_0}{\omega} = -0.235 \\ K_2 &= \frac{d_{12}^2 \mathcal{E}_0^2}{\omega^2} = 0.0138 \\ K_3 &= -\frac{d_{13}^2 \mathcal{E}_{L2}^2 \sqrt{\pi} \sigma_{L2}}{4} \sim -3.54 \times 10^7 \text{ rad/s} \\ K_4 &= d_{12} \sqrt{\frac{\pi}{a}} = -0.0078 \text{ rad/}[\text{s}^{\frac{3}{2}}(\text{V/m})] \\ T &= \mathcal{T} + t_{diff} \sim 10^{-4} \text{ s} \\ \phi &= T_e/2 = \pi/\omega \\ a &= \frac{v^2}{2\sqrt{2}\sigma_u^2} \sim 2.3 \times 10^9 \text{ 1/s}^2 \end{aligned}$$

Eqn. (2.62) can be written as a function of  $\Delta, \delta_{L2}, \mathcal{E}_{nr,0}$  with cleaner notation:

$$\begin{aligned} c_+^{(2,N=1,1)}(\Delta, \delta_{L2}, \mathcal{E}_{nr,0}, \mathcal{E}_0) &= K_1 e^{-i\Delta\phi} \sin(\Delta\phi) - i \left( 1 + K_2 (e^{i2\phi\Delta} - 1) \right) \\ &\quad \times \exp\left(\frac{iK_3}{\delta_{L2} - i\frac{\Gamma}{2}}\right) \mathcal{E}_{nr,0} K_4 e^{-i\Delta T - \Delta^2/4a} \\ &\approx K_1 e^{-i\Delta\phi} \sin(\Delta\phi) + \mathcal{E}_{nr,0} K_4 e^{-i\Delta T - i\pi/2 - \Delta^2/4a + \frac{iK_3}{\delta_{L2} - i\frac{\Gamma}{2}}} \end{aligned} \quad (2.63)$$

$$\equiv A + B \quad (2.64)$$

where in the second equation, I return to the first order TDPT result in Region 1, and absorb  $-i$  into the exponential. We have also defined

$$A = K_1 e^{-i\Delta\phi} \sin(\Delta\phi) \quad (2.65)$$

$$B = \mathcal{E}_{\text{nr},0} K_4 e^{-i\Delta T - i\pi/2 - \Delta^2/(4a) + \frac{iK_3}{\delta_{L2} - i\Gamma/2}} \quad (2.66)$$

Now compute the magnitude square of this amplitude to get the approximated population. Since

$$c_+ = A + B = |A| e^{i\theta_A} + |B| e^{i\theta_B} \quad (2.67)$$

we have

$$S(\Delta, \delta_{L2}, \mathcal{E}_{\text{nr},0}, \mathcal{E}_0) = |c_+|^2 = |A|^2 + |B|^2 + 2|A||B| \cos(\theta_A - \theta_B). \quad (2.68)$$

It's obvious to see that  $|A| = K_1 \sin(\Delta\phi)$  with the phase  $\theta_A = -\Delta\phi$ . For  $B$ , we note that

$$\exp\left(\frac{iK_3}{\delta_{L2} - i\Gamma/2}\right) = \exp\left(\frac{K_3 \Gamma/2}{\delta_{L2}^2 + (\Gamma/2)^2}\right) \exp\left(i \frac{K_3 \delta_{L2}}{\delta_{L2}^2 + (\Gamma/2)^2}\right) \quad (2.69)$$

$$= \alpha e^{i\beta} \quad (2.70)$$

where we have define

$$\alpha = \exp\left(\frac{K_3 \Gamma/2}{\delta_{L2}^2 + (\Gamma/2)^2}\right) \quad (2.71)$$

$$\beta = \frac{K_3 \delta_{L2}}{\delta_{L2}^2 + (\Gamma/2)^2} \quad (2.72)$$

Therefore, the magnitude of  $B$

$$|B| = \mathcal{E}_{\text{nr},0} K_4 e^{-\Delta^2/(4a)} \alpha \quad (2.73)$$

and the phase

$$\theta_B = -\Delta T - \pi/2 + \beta \quad (2.74)$$

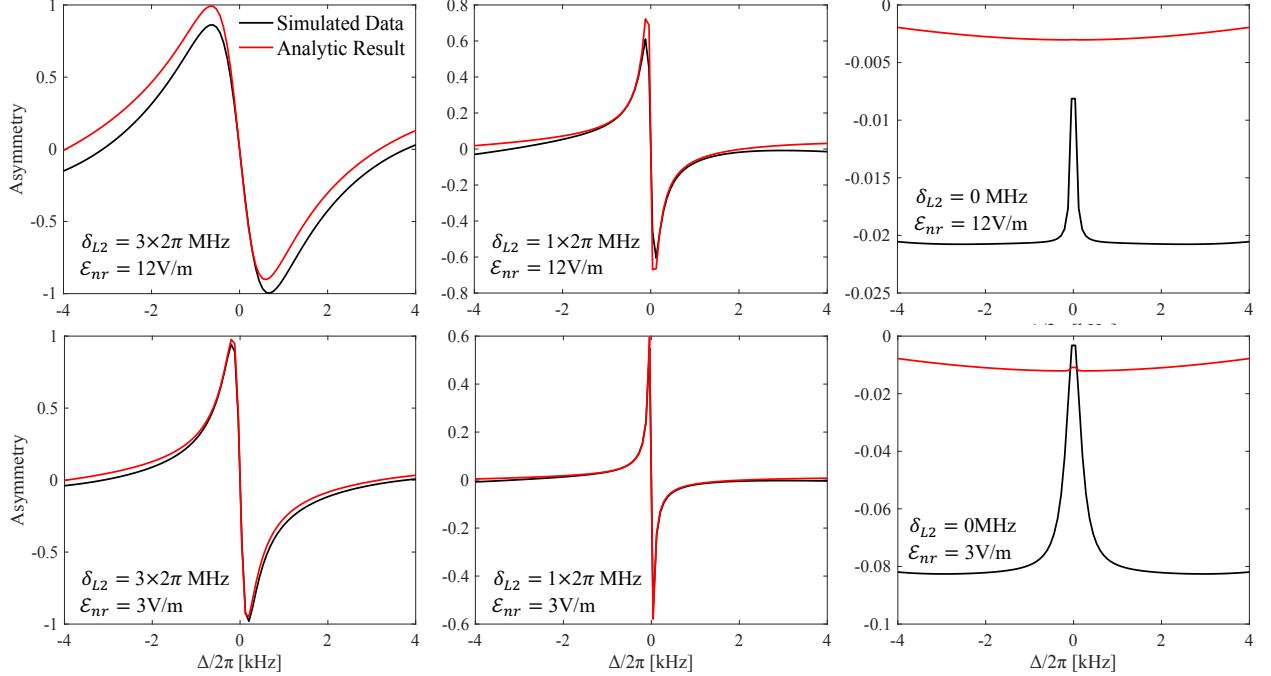


Figure 2.10: Comparison of asymmetry curves obtained from numerical simulation (black) and analytic model in Eqn. (2.76) (red), using parameters listed in Table (2.1). The analytic model shows good agreement with the simulation across all cases, apart from a constant vertical offset. This offset manifests as a discrepancy in the extracted  $a_0$  values, as will be further discussed in Figure (2.11).

Thus, the population

$$S = K_1^2 \sin^2(\Delta\phi) + \mathcal{E}_{nr,0}^2 K_4^2 e^{-\Delta^2/(2a)} \alpha + 2K_1 K_4 \mathcal{E}_{nr,0} \sin(\Delta\phi) e^{-\Delta^2/(4a)} \alpha \cos\left[\Delta(T - \phi) + \frac{\pi}{2} - \beta\right] \quad (2.75)$$

By noting that in the above expression, the only odd term under reverse  $\mathcal{E}_0$  is the last term. Therefore, using definition in Eqn. (2.29), we obtain an analytical expression for the asymmetry:

$$\mathcal{A}_{\text{analytic}}(\Delta) = \frac{-2K_1 K_4 \mathcal{E}_{nr,0} \sin(\Delta\phi) e^{-\Delta^2/(4a)} \alpha \sin\left[\Delta(T - \phi) - \beta\right]}{K_1^2 \sin^2(\Delta\phi) + \mathcal{E}_{nr,0}^2 K_4^2 e^{-\Delta^2/(2a)} \alpha^2} \quad (2.76)$$

## Analytic Expressions for $W, a_0$ , and $a_1$

We want to map our analytic expression Eqn. (2.76) to our fitting function Eqn. (1.2) to obtain an analytic expressions for the fitting parameters  $W, a_0$ , and  $a_1$ . The idea is to use Taylor expansion on both the fitting function and our analytic function for asymmetry as function of  $\Delta$ , and compare the terms and hopefully extract expressions for those constants. Recall our fitting function is written as

$$\mathcal{A}_{\text{fit}}(\Delta) = 2 \frac{W \omega^2 - \Delta^2}{\Delta} \frac{\sin\left(\frac{\Delta}{2}(T_e + T_{f1} + T_{f2})\right)}{\sin(\Delta T_e/2)} \cos\left(\frac{\Delta}{2}(T_{f1} - T_{f2})\right) + a_0 + a_1 \cdot \Delta \quad (2.77)$$

Using trigonometry identity  $\sin A \cos B = \frac{1}{2}(\sin(A+B) + \sin(A-B))$ , we can write

$$\begin{aligned} \mathcal{A}_{\text{fit}}(\Delta) &= \frac{W \omega^2 - \Delta^2}{\Delta} \frac{\sin\left(\Delta(T_e/2 + T_{f2})\right) + \sin\left(\Delta(T_e/2 + T_{f1})\right)}{\sin(\Delta T_e/2)} + a_0 + a_1 \cdot \Delta \\ &\approx \frac{W}{\Delta} \frac{2\omega}{d_{12} \cdot \mathcal{E}_0} \frac{\mathcal{T}}{T_e} + a_0 + a_1 \cdot \Delta \\ &\equiv \frac{a_{-1}}{\Delta} + a_0 + a_1 \cdot \Delta + \mathcal{O}(\Delta^2) \end{aligned} \quad (2.78)$$

where we define  $a_{-1} = \frac{2W\omega}{d_{12} \cdot \mathcal{E}_0} \frac{\mathcal{T}}{T_e}$ . However, direct expansion of Eqn. (2.76) would give us a linear term  $\mathcal{O}(\Delta)$  to the lowest order, instead of  $\mathcal{O}(\Delta^{-1})$  as for the fitting function Eqn. (2.78). This is because for  $\Delta \rightarrow 0$ , Eqn. (2.76) goes linearly with  $\Delta$ , instead exploding like the fitting function. To fix this issue, we note that since our fitting function only fit the data between  $1\text{MHz} < |\Delta| < 4\text{MHz}$ , we should really work in the regime where  $|\Delta| > 1\text{MHz}$ . Now the Eqn. (2.76) simplifies to:

$$\begin{aligned} \mathcal{A}_{\text{analytic}}(\Delta) &\approx \frac{-2\alpha K_4 \mathcal{E}_{\text{nr},0} e^{-\Delta^2/(4a)}}{K_1 \sin(\Delta\phi)} \sin\left[\Delta(T - \phi) - \beta\right] \\ &= \frac{\gamma e^{-\Delta^2/(4a)} \sin\left[\Delta(T_e/2 + T_{f1} + T_{f2} + t_{\text{diff}}) - \beta\right]}{\sin(\Delta T_e/2)} \end{aligned} \quad (2.79)$$

where  $\gamma = \frac{-2\alpha K_4 \mathcal{E}_{\text{nr},0}}{K_1}$ . Now, using Mathematica to do the series expansion of  $\mathcal{A}_{\text{analytic}}(\Delta)$  around  $\Delta = 0$  up to order  $\mathcal{O}(\Delta)$  we have

$$\begin{aligned}\mathcal{A}_{\text{analytic}}(\Delta) &= -\frac{2\gamma \sin \beta}{\Delta T_e} + \frac{\gamma(2t_{\text{diff}} + T_e + 2(T_{f2} + T_{f1})) \cos \beta}{T_e} \\ &\quad + \Delta \gamma \left[ \left( \frac{1}{a T_e} - \frac{T_e}{12} \right) + \frac{(2t_{\text{diff}} + T_e + 2(T_{f2} + T_{f1}))^2}{4T_e} \right] \sin \beta + \mathcal{O}(\Delta^2) \\ &= \frac{c_{-1}}{\Delta} + c_0 + c_1 \cdot \Delta + \mathcal{O}(\Delta^2)\end{aligned}\tag{2.80}$$

Now all we need to do is to make  $\mathcal{A}_{\text{analytic}}(\Delta) = \mathcal{A}_{\text{sim}}(\Delta)$  by matching the coefficients at each order of  $\Delta$ , namely:

$$a_{-1} = c_{-1}\tag{2.81}$$

$$a_0 = c_0\tag{2.82}$$

$$a_1 = c_1\tag{2.83}$$

Consider  $a_{-1} = c_{-1}$ , we have

$$\frac{2W\omega}{d_{12} \cdot \mathcal{E}_0} \frac{\mathcal{T}}{T_e} = -\frac{2\gamma \sin \beta}{T_e}\tag{2.84}$$

rearrange we have

$$\begin{aligned}W(\delta_{L2}, \mathcal{E}_{\text{nr},0}) &= \frac{-d_{12}\mathcal{E}_0\gamma \sin \beta}{\omega \mathcal{T}} \\ &= \frac{2\alpha K_4 d_{12} \mathcal{E}_0 \mathcal{E}_{\text{nr},0} \sin \beta}{\omega K_1 \mathcal{T}} \\ &= \frac{d_{12} \mathcal{E}_{\text{nr},0}}{\mathcal{T}} \sqrt{\frac{\pi}{a}} \exp\left(\frac{K_3 \Gamma/2}{\delta_{L2}^2 + (\Gamma/2)^2}\right) \sin\left(\frac{K_3 \delta_{L2}}{\delta_{L2}^2 + (\Gamma/2)^2}\right) \\ &\approx \frac{4d_{12} K_3 \mathcal{E}_{\text{nr},0} \delta_{L2}}{\Gamma^2 \mathcal{T}} \sqrt{\frac{\pi}{a}} \exp\left(\frac{K_3 \Gamma/2}{\delta_{L2}^2 + (\Gamma/2)^2}\right)\end{aligned}\tag{2.85}$$

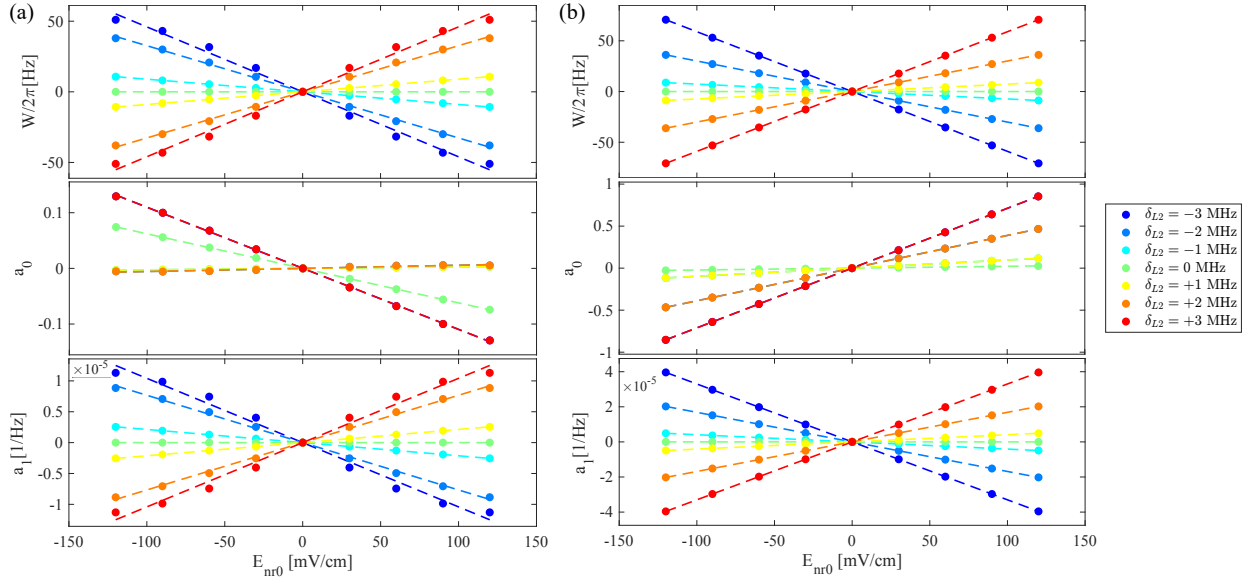


Figure 2.11: Calculated Error signal  $W$ ,  $a_0$ , and  $a_1$  extracted from (a) numerical simulation, and (b) analytic expressions Eqn. (2.85)-Eqn. (2.87).

Similarly, for  $a_0 = c_0$ , we get

$$\begin{aligned}
 a_0(\delta_{L2}, \mathcal{E}_{nr,0}) &= \frac{\gamma(2t_{\text{diff}} + T_e + 2(T_{f2} + T_{f1})) \cos \beta}{T_e} \\
 &= \frac{-\omega \mathcal{E}_{nr,0}(2t_{\text{diff}} + 2\mathcal{T} - T_e)}{\mathcal{E}_0 T_e} \sqrt{\frac{\pi}{a}} \exp\left(\frac{K_3 \Gamma/2}{\delta_{L2}^2 + (\Gamma/2)^2}\right) \cos\left(\frac{K_3 \delta_{L2}}{\delta_{L2}^2 + (\Gamma/2)^2}\right) \\
 &\approx \frac{-\omega \mathcal{E}_{nr,0}(2t_{\text{diff}} + 2\mathcal{T} - T_e)}{\mathcal{E}_0 T_e} \sqrt{\frac{\pi}{a}} \exp\left(\frac{K_3 \Gamma/2}{\delta_{L2}^2 + (\Gamma/2)^2}\right)
 \end{aligned} \tag{2.86}$$

For  $a_1 = c_1$  we have

$$\begin{aligned}
 a_1(\delta_{L2}, \mathcal{E}_{nr,0}) &= \frac{-\omega \mathcal{E}_{nr,0}}{\mathcal{E}_0} \sqrt{\frac{\pi}{a}} \left[ \left( \frac{1}{a T_e} - \frac{T_e}{12} \right) + \frac{(2t_{\text{diff}} + 2\mathcal{T} - T_e)^2}{4T_e} \right] \\
 &\quad \times \exp\left(\frac{K_3 \Gamma/2}{\delta_{L2}^2 + (\Gamma/2)^2}\right) \sin\left(\frac{K_3 \delta_{L2}}{\delta_{L2}^2 + (\Gamma/2)^2}\right) \\
 &\approx \frac{-4\omega K_3 \mathcal{E}_{nr,0} \delta_{L2}}{\mathcal{E}_0 \Gamma^2} \sqrt{\frac{\pi}{a}} \left[ \left( \frac{1}{a T_e} - \frac{T_e}{12} \right) + \frac{(2t_{\text{diff}} + 2\mathcal{T} - T_e)^2}{4T_e} \right] \exp\left(\frac{K_3 \Gamma/2}{\delta_{L2}^2 + (\Gamma/2)^2}\right)
 \end{aligned} \tag{2.87}$$

### 2.2.3 Comparison Between Simulation and Analytic Result